Matter

CellPress

Article

# Strong Plasmon-Wannier Mott Exciton Interaction with High Aspect Ratio Colloidal Quantum Wells

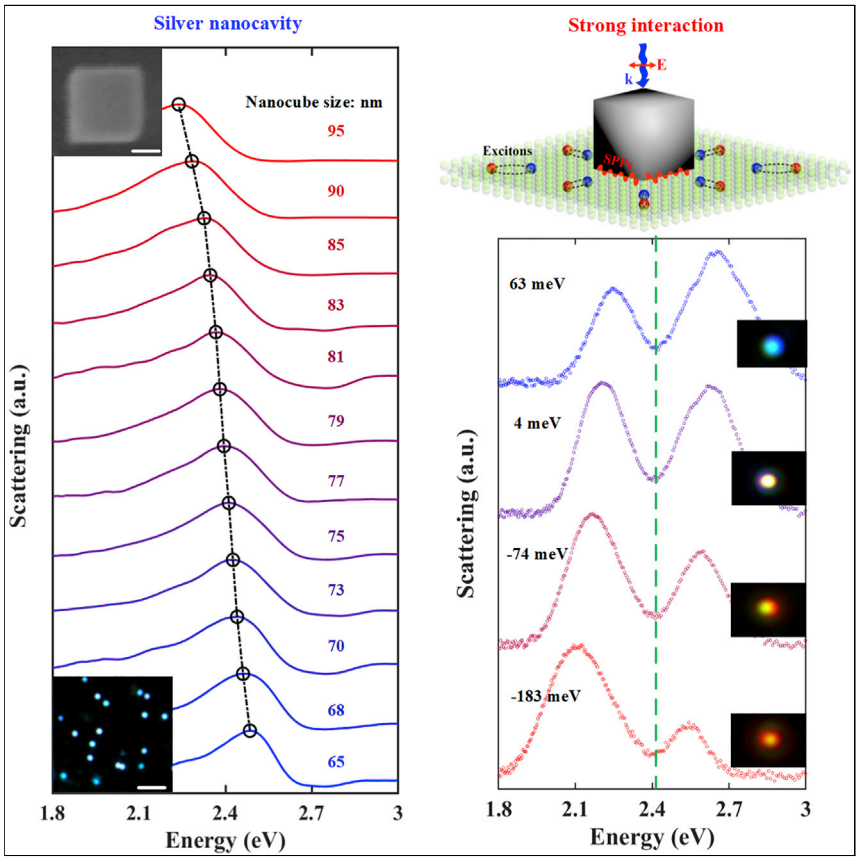


Wannier Mott excitons are preferred for the development of plasmon-polariton devices compared with Frenkel excitons. However, the weak interaction between inorganic materials and plasmons restricts the potential capability of active plasmonic operation. Here, utilizing high aspect ratio colloidal quantum wells, an unprecedented giant Rabi splitting energy with high cooperativity has been demonstrated.

Junhong Yu, Songyan Hou, Manoj Sharma, ..., Hong Wang, Hilmi Volkan Demir, Cuong Dang

mbirowosuto@ntu.edu.sg (M.D.B.)
volkan@stanfordalumni.org (H.V.D.)
hcdang@ntu.edu.sg (C.D.)

## HIGHLIGHTS

A giant Rabi energy in inorganic exciton-plasmon coupling has been achieved

The microscopic origin of the strong interaction is examined

Inorganic colloidal quantum wells have great potential for polaritonic devices

**Demonstrate**
Proof-of-concept of performance with intended application/response

Yu et al., Matter 2, 1–14
June 3, 2020 
https://doi.org/10.1016/j.matt.2020.03.013

Please cite this article in press as: Yu et al., Strong Plasmon-Wannier Mott Exciton Interaction with High Aspect Ratio Colloidal Quantum Wells, Matter (2020), https://doi.org/10.1016/j.matt.2020.03.013

Matter

CellPress

Article

# Strong Plasmon-Wannier Mott Exciton Interaction with High Aspect Ratio Colloidal Quantum Wells

Junhong Yu,[1,6] Songyan Hou,[2,6] Manoj Sharma,[1,5] Landobasa Y.M. Tobing,[3] Zhigang Song,[3] Savas Delikanli,[1,5] Chathuranga Hettiarachchi,[3] Daohua Zhang,[1,3] Weijun Fan,[3] Muhammad Danang Birowosuto,[2,*] Hong Wang,[2] Hilmi Volkan Demir,[1,4,5,*] and Cuong Dang[1,2,3,7,*]

## SUMMARY

**The strong interaction between excitons and plasmons, manifested as Rabi splitting of the eigen energies, is of fundamental interest for manipulating photons in nanoscale devices. Thanks to their enhanced photostability and minimal inhomogeneous broadening compared with organic molecules, inorganic emitters are preferred for practical applications. However, a relatively small Rabi splitting with inorganic materials severely hinders the active plasmonic operation, considering its weak optical nonlinearity and slow energy interexchange. Here, we circumvent this problem in a hybrid system consisting of high aspect ratio colloidal quantum wells (HARCQWs) and an individual plasmonic silver nanocube. By taking advantages of a highly in-plane oriented exciton, enhanced exciton binding energy, and non-stacking properties in HARCQWs, we demonstrate an unprecedented giant Rabi splitting energy up to 400 meV under ambient conditions, which is observed not only in scattering but also in photoluminescent spectra. These findings are a key step toward achieving inorganic plasmonic devices.**

## INTRODUCTION

Interaction between excitons and localized surface plasmons (LSPs) sustained in metallic nanostructures is at the heart of future nanodevice research in view of deep subwavelength confinement of the electromagnetic fields,[1–4] which allows size scalability and open cavity configuration[5–10], ensuring easy access to probe/manipulate light-matter coupling. If the coherent energy exchange rate between excitons and LSPs is faster than any other dissipative dynamics, the most intriguing regime, the so-called strong interaction, is achieved.[11–13] In this regime, there is a change from irreversible spontaneous emission (Purcell effect)[14] to a reversible energy exchange (Rabi splitting) between excitons and LSPs.[5,9,11–13] This regime can be categorized into individual and collective Rabi splitting. Individual Rabi splitting pushes the interaction toward the quantum optics limit to enable light control at the single-photon level, which is appreciated by quantum networks and quantum information processing.[1,3] Collective Rabi splitting brings quantum effects to a macroscopic scale and is highly desirable for ultrafast optical switches[1,3] and thresholdless polariton lasers.[2,14] From the plasmonic application perspective, Rabi splitting energy is a key figure of merit.[9,15–17] Systems with large Rabi splitting have several promising properties, including strong coupling strength, enhanced optical nonlinearity, and ultrafast coherent energy exchange.[1,12,18]

### Progress and Potential

Exciton-plasmon strong coupling utilizing inorganic emitters has sparked great research enthusiasm, because compared with organic molecules (Frenkel excitons), Wannier Mott excitons offer high levels of optical stability, suppressed emission broadening, and endurance of high photon density. However, achieving similar coupling strength to that observed in organic materials using Wannier Mott excitons is still a daunting challenge.

Here, by using an open plasmonic nanocavity, a giant Rabi splitting (>400 meV) with high cooperativity (>11) in the Wannier Mott exciton-plasmon interaction has been demonstrated thanks to an enhanced exciton binding energy, non-stacking properties, and the face-down geometry of high aspect ratio colloidal quantum wells.

Combining fast coherent energy transfer cycle with fully solution-processed, optical-stable inorganic emitters, our result may have a major impact on plasmonic devices.

To overcome the fast dissipation of plasmonic mode in metallic nanostructures, organic molecules that exhibit giant oscillator strength and large absorption cross-section are commonly reported emitters to attain a strong coupling regime.[19–29] Recent studies have demonstrated strong exciton-plasmon interaction involving both multiple molecules and a single molecule. To date, Shegai et al.[25] observed a Rabi splitting of ~400 meV using multiple J-aggregate molecules and a silver nanoprism. Wang et al.[29] achieved strong interaction between a single J-aggregate molecule and a gold nanorod with a Rabi splitting of ~42 meV. However, organic molecules have limited photostability, large inhomogeneous broadening, and are prone to emission bleaching.[30] These issues have severely hindered the practical applications of organic-plasmonic systems.

Inorganic colloidal nanomaterials, which not only retain the strength of organic molecules (e.g., solution processability and scalability) but also possess a number of advantages over organic molecules (e.g., optical stability, suppressed emission broadening, and endurance of high photon density),[31–33] have emerged as another promising class of materials for strong exciton-plasmon interaction. Quasi-two-dimensional (2D) CdSe colloidal quantum wells (CQWs),[34] as colloidal counterparts of epitaxial quantum wells, offer superior properties that can benefit the exciton-plasmon interaction. Compared with other 0D (quantum dots) and 1D (nanowires, nanorods) colloidal nanomaterials, CQWs exhibit extremely narrow emission linewidth (<40 meV) due to vertical thickness control at the mono-atomic level[34,35] and significantly enhanced absorption coefficients (~$3 \times 10^7$ $cm^{-1}$ in CQWs versus ~$2 \times 10^4$ $cm^{-1}$ in quantum dots) resulting from increased exciton center-of-mass extension.[34,36] Just 10 months ago, for the first time, Norris et al.[15] demonstrated a strong exciton-plasmon interaction using CdSe CQWs and a metallic photonic crystal. However, due to the relatively low exciton binding energy, imperfectly matched exciton dipole orientation with respect to electric field distribution, and fast non-radiative dissipative dynamics (i.e., Förster resonance energy transfer [FRET]) in a dense film, the Rabi splitting energy observed in a CQW-metal system is only 110 meV, even smaller than the value reported in colloidal quantum dots (up to 160 meV).[17,37]

Generally, Rabi splitting energy ($\hbar\Omega$) is in accordance with $\hbar\Omega = 2g \propto \sqrt{fN/V}$,[12,13] where $g$ is the coupling strength, $f$ is the oscillation strength of the exciton, $V$ is the optical mode volume, and $N$ is the saturated concentration of excitons involved in strong coupling. Here, to achieve ultra-strong exciton-plasmon interaction, we utilize the high aspect ratio colloidal quantum wells (HARCQWs) with one lateral size tailored down to ~6 nm (the exciton Bohr radius in CdSe, ~ 5.7 nm)[38] as the exciton source. The greatly enhanced exciton binding energy resulting from an additional quantum confinement dimension and inefficient FRET due to non-stacking properties[39–41] in the HARCQW assembly are beneficial to improve the oscillator strength. Furthermore, we achieved a face-down HARCQW assembly due to weak van der Waals interactions[39–41] between HARCQWs to ensure the maximum overlap (effective $N$) between the exciton dipole orientation and the electric field in LSPs. For the plasmon part, instead of using top-down metallic nanostructures fabricated by lithography, we adopted solution-processable colloidal silver nanocubes of different sizes to tune the resonance energy.[42] The anti-crossing behavior of two polaritonic states in dark-field scattering measurements shows a giant Rabi splitting energy exceeding 400 meV (corresponds to 0.1 $fs^{-1}$ energy transfer rate). To the best of our knowledge, this is the largest Rabi splitting observed in any Wannier Mott exciton and plasmon system. Moreover, the photoluminescence spectra of the hybrid system arising from the low polariton branch further demonstrate ultrafast

[1]LUMINOUS! Centre of Excellence for Semiconductor Lighting and Displays, School of Electrical and Electronic Engineering, The Photonics Institute (TPI), Nanyang Technological University, 50 Nanyang Avenue, Singapore 639798, Singapore

[2]CINTRA UMI CNRS/NTU/THALES 3288, Research Techno Plaza, 50 Nanyang Drive, Border X Block, Level 6, Singapore 637553, Singapore

[3]Centre for OptoElectronics and Biophotonics, School of Electrical and Electronic Engineering, The Photonics Institute (TPI), Nanyang Technological University, 50 Nanyang Avenue, Singapore 639798, Singapore

[4]School of Physical and Mathematical Sciences, Nanyang Technological University, Singapore 639798, Singapore

[5]Departments of Electrical and Electronics Engineering, and Physics, UNAM-Institute of Materials Science and Nanotechnology, Bilkent University, Bilkent, Ankara 06800, Turkey

[6]These authors contributed equally

[7]Lead Contact

*Correspondence: mbirowosuto@ntu.edu.sg (M.D.B.), volkan@stanfordalumni.org (H.V.D.), hcdang@ntu.edu.sg (C.D.)

https://doi.org/10.1016/j.matt.2020.03.013

Please cite this article in press as: Yu et al., Strong Plasmon-Wannier Mott Exciton Interaction with High Aspect Ratio Colloidal Quantum Wells, Matter (2020), https://doi.org/10.1016/j.matt.2020.03.013



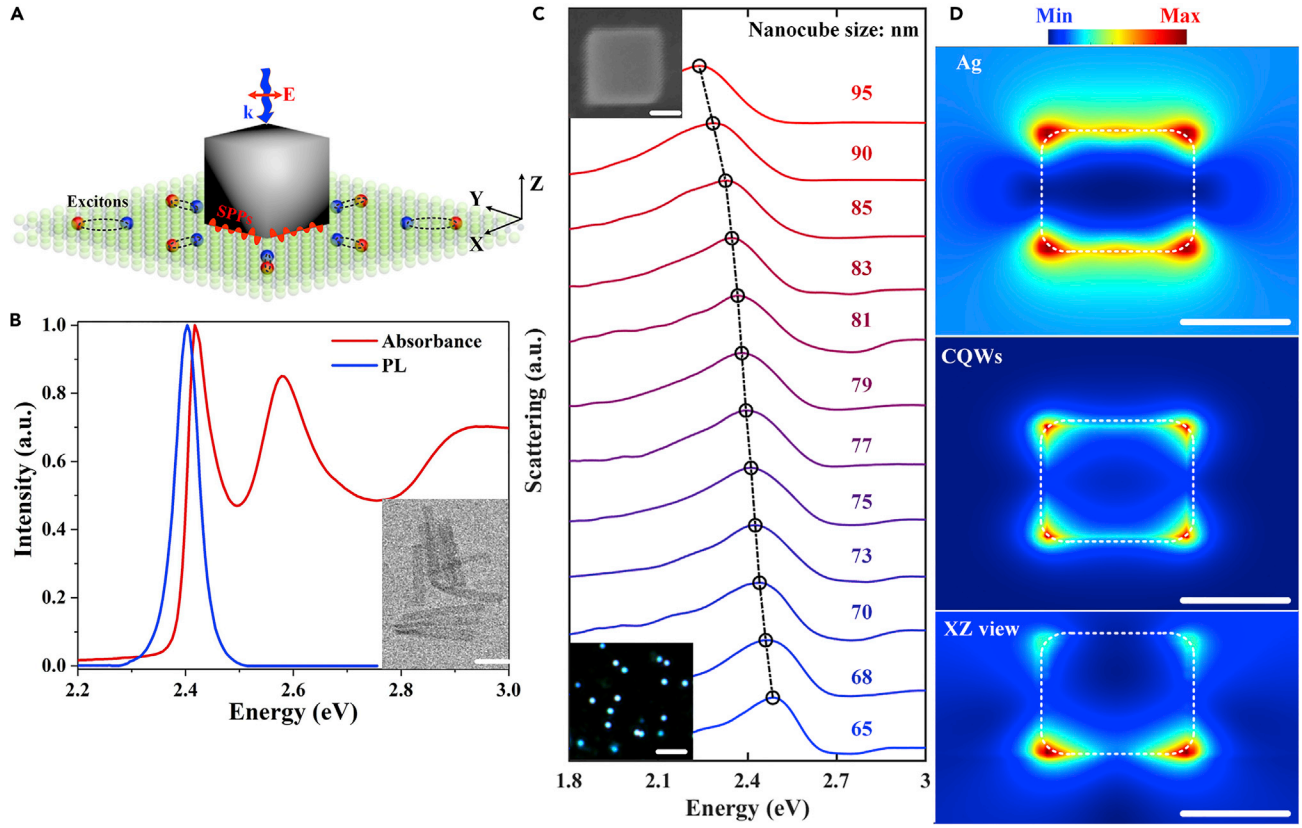


**Figure 1. The Hybrid Exciton-Plasmon System**

(A) A schematic showing the hybrid system consisting of an individual silver nanocube coupled to the densely packed HARCQW film. The excitons and LSPs are excited by the TM-polarized white light. TM polarization is defined by the electric field along the *X* direction.

(B) Normalized photoluminescence (blue) and absorbance (red) spectra of HARCQWs dispersed in hexane. Inset: TEM image of CQWs indicating the high aspect ratio. Scale bar, 25 nm.

(C) Scattering spectra measured for silver nanocubes of varying size. As the size of the nanocube increases, the LSP peak (black circles) shifts to lower energies as highlighted by the dashed line. Top inset: SEM image of an individual 75-nm silver nanocube. Scale bar, 50 nm. Bottom inset: dark-field scattering image of silver nanocubes over the $SiO_2$/Si substrate illuminated by TM-polarized light. Scale bar, 1 μm.

(D) Near-field electric-field intensity distribution of an individual silver nanocube over the densely packed HARCQW film. The contours are normalized by the incident electric field and correspond to the LSP peak (2.41 eV) of a 75-nm silver nanocube. Upper: electric field distribution in the silver nanocube, top view (*XY* plane), Middle: electric field distribution in the HARCQW film, top view (*XY* plane), Lower: electric field distribution in the HARCQW film, side view (*XZ* plane). White dashed lines outline the silver nanocube. Scale bar, 50 nm.

coherent energy exchange between excitons and plasmons. These results provide a way to explore practical applications of bottom-up and small footprint exciton-plasmon polariton nanodevices.

## RESULTS

### The Strong Plasmon-Exciton Interaction

Hybrid plasmon-exciton systems are produced experimentally as illustrated in Figure 1A. Transverse magnetic (TM) polarized light excites both LSPs in the silver nanocube and Wannier Mott excitons in HARCQWs. Here, we only consider in-plane (i.e., in the XY plane) LSP mode because the near-field electric field enhancement of out-of-plane LSP mode is one to two orders of magnitude weaker.[6,42,43] When the LSP resonance crosses the excitonic transition (spectral overlap), and the exciton dipoles align with the enhanced near-field in-plane plasmonic mode (spatial overlap), a strong plasmon-exciton interaction (mode splitting) can be most likely achieved.[2,13]

Please cite this article in press as: Yu et al., Strong Plasmon-Wannier Mott Exciton Interaction with High Aspect Ratio Colloidal Quantum Wells, Matter (2020), https://doi.org/10.1016/j.matt.2020.03.013



The exciton components of the hybrid system are shown in Figure 1B. Four monolayer (4 ML) CdSe CQWs were synthesized with the previous recipes,[34,35] which we optimized to obtain a desirable aspect ratio here (see details in Experimental Procedures). Transmission electron microscopy (TEM) characterization of the CQWs (the inset in Figure 1B) reveals that they are approximately rectangular shape with an aspect ratio as large as ten to one (lateral size, ~50 nm by 5–8 nm; see the lateral size deviation of CQWs in Figure S1). Also, the quantum yield (QY) is around 55%, suggesting negligible cracking or strain in these HARCQWs. The absorption peaks (heavy-hole transition, 2.417 eV; light-hole transition, 2.578 eV), emission peak (2.413 eV), and linewidths (~40 meV) of the HARCQWs are consistent with the values reported previously for those low aspect ratio CdSe CQWs.[34,36,39–41] Considering additional confinement along the lateral direction in HARCQWs, the independent relationship between the excitonic transitions and aspect ratios means that a larger exciton binding energy can be expected in HARCQWs, which is discussed further in Figure 3. Typically, there is a square-root dependence of the Rabi energy on the number of dipoles coupled to the LSP mode ($\hbar\Omega \propto \sqrt{N}$).[15,29] For this reason, densely packed HARCQW film is preferred to achieve large mode splitting. However, the Rabi energy cannot be endlessly enhanced by increasing the film thickness due to the exponentially decaying intensity of the LSP mode (in the Z direction, the penetration length of the electric field of the LSP mode is ~100 nm in the green spectral range).[3,15] Thus, beyond the saturation condition (i.e., thickness >100 nm), increasing the film thickness should not further enhance the Rabi energy because the excitons no longer experience the LSP mode.[15] Here, we drop-casted HARCQWs dissolved in hexane onto Si substrate with a 100 nm thermally grown $SiO_2$ film. The thickness of the HARCQW film was controlled by varying the concentration in hexane while fixing the drop-cast area. The thickness of the HARCQW film experimentally investigated extended to 400 nm, which is already beyond the penetration depth of LSP mode.

Another component of the hybrid system is the metallic nanocavity. In this study, we chose a silver nanocube, considering that gold is limited to operating with photon energies below the heavy-hole exciton transition (~2.4 eV).[44] These silver nanocubes composed of a polyvinylpyrrolidone layer (2–3 nm) to avoid oxidation were purchased from Nanocomposix.[45] To ensure only one nanocube was characterized and mapped, very diluted nanocubes dispersed in ethanol (1,000 times of the commercial concentration) were sparsely deposited onto the $SiO_2$/Si substrate or the densely packed HARCQW film via spin-casting. Multiple individual silver nanocubes in a square area of 100 μm × 100 μm were characterized by dark-field scattering spectroscopy (see the details in Experimental Procedures) and their locations were optically imaged/labeled according to the large surface features over the $SiO_2$/Si substrate (see Figure S2). Then, each specific nanocube was imaged using scanning electron microscopy (SEM) to extract size information and exclude clusters or distorted nanocubes. The scattering spectra of an individual nanocube over $SiO_2$/Si substrate (in the absence of HARCQWs) of varied sizes are presented in Figure 1C, confirming the spectral overlap of each nanocube with the HARCQW heavy-hole exciton peak (2.42 eV). In particular, the scattering spectrum shifts from 2.49 to 2.24 eV as the size of the nanocubes increases from 65 to 95 nm due to the retardation effect,[42] accompanied by a broader spectral profile (see the SEM images of nanocubes with varied size and linewidths, and changes in the scattering spectra in Figure S3). A scattering image of an example area is shown in the bottom inset of Figure 1C; nanocubes are isolated and appear cyanish under TM illumination.

To fully understand the plasmon-exciton interaction in such a hybrid system, we computed the near-field electric field intensity distribution using finite-difference

Please cite this article in press as: Yu et al., Strong Plasmon-Wannier Mott Exciton Interaction with High Aspect Ratio Colloidal Quantum Wells, Matter (2020), https://doi.org/10.1016/j.matt.2020.03.013



time-domain modeling (see Note S1). The separation between the nanocubes and HARCQWs is estimated to be ~4–6 nm according to the organic ligand length of the HARCQWs (2–3 nm)[34,46] and the thickness of the polyvinylpyrrolidone protective layer covering the nanocubes. The computed electric field map corresponding to photon energy of 2.41 eV is shown in Figure 1D. As can be seen, the electric field sustained by the silver nanocube is highly confined around the sharp edges, significantly reducing the optical mode volume of the nanocubes. We also observe that the electric field intensities effectively localize in the HARCQW layer (spatial overlap) in both the top and the side views. Thus, the hybrid system with a small optical mode volume together with the large overlap between the plasmonic fields and the excitons should be an excellent breeding ground for a strong exciton-plasmon interaction.

Here, we demonstrate experimentally that the silver nanocube-HARCQW hybrid system enters a strong coupling regime by measuring its dark-field scattering spectra. As previously discussed in Figure 1C, silver nanocubes ranging in size from 65 to 95 nm allow us to detune the plasmon resonance energy between +63 and −183 meV, crossing the heavy-hole exciton transition at 2.42 eV. Four representative scattering spectra for hybrid systems with different detuning energies ($\delta = E_{plasmon} - E_{ex}$) are presented in Figure 2A, in which the transparency dip (highlighted by the dashed green line) covering the heavy-hole exciton transition clearly indicates two prominent hybrid modes (upper polariton branch [UPB] and lower polariton branch [LPB]). Specifically, as the detuning energy changes from positive to negative, the LPB overwhelms the UPB and the scattering spectra shifts to the red region. This trend can also be observed in the dark-field scattering microscopy images; as plasmon energy decreases, the color of the silver nanocube changes from bluish to reddish. In particular, as the detuning energy is close to zero, the intensities of the UPB and the LPB are comparable with each other, and the dark-field scattering image looks whitish.

The anti-crossing behavior can be seen more clearly on the contour map of the normalized scattering spectra (Figure 2B). First, the dispersionless dip is exactly located at energy of ~2.41 eV (white dashed line), which corresponds to the electron-heavy-hole transition in HARCQWs. In addition, two peaks associated with the LPB and the UPB are dispersive as expected following the detuning change. Furthermore, these experimental data can be corroborated with numerical simulations to verify the exciton-plasmon interaction in the hybrid system. As shown in Figure 2C, we utilized coupled harmonic oscillator mode[16,18,47,48] (see Note S2) to reproduce the dispersions of the peak energies of the hybrid states and thus, extract the coupling strength and the Rabi energy. From both the experimental contour map of the scattering spectra (Figure 2B) and the phenomenological model (Figure 2C), we can unambiguously conclude that as the plasmon resonance energy varies across the heavy-hole exciton transition, the scattering spectrum splits into two polariton bands, exhibiting a distinct anti-crossing behavior with a giant Rabi splitting of ~402 meV. This Rabi energy is the highest value ever reported for Wannier Mott exciton-plasmon interaction systems, which indicates an ultrafast energy transfer cycle[47,49] with a corresponding rate of ~0.1 $fs^{-1}$ and implies a giant interaction strength[48] with Rabi energy exceeding 15% of the excitonic energy.

More insight into the nature of light-matter interaction of our hybrid system can be obtained by investigating the coupling strength ($g$). Here, we adopt the strictest criterion, $(2g)^2 > \gamma_{LSP}^2 + \gamma_{hl\text{-}ex}^2$, to indicate that the strong coupling regime has been reached, in comparison with $2g > (\gamma_{LSP} + \gamma_{hl\text{-}ex})/2$ or $2g > \gamma_{LSP}$ used in previous

Please cite this article in press as: Yu et al., Strong Plasmon-Wannier Mott Exciton Interaction with High Aspect Ratio Colloidal Quantum Wells, Matter (2020), https://doi.org/10.1016/j.matt.2020.03.013



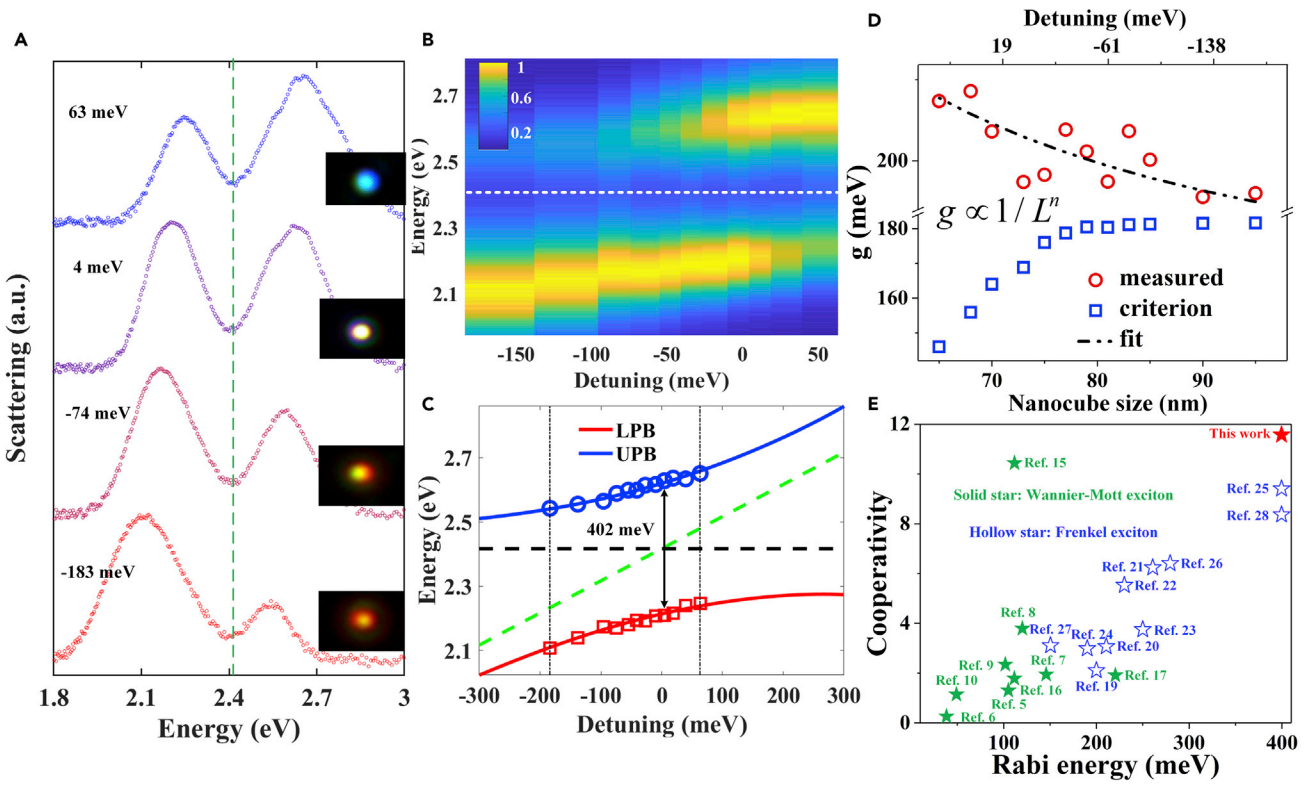


**Figure 2. Strong Coupling in the Silver Nanocube-HARCQW Hybrid System**

(A) Normalized dark-field scattering spectra for −183, −74, 4, and 63 meV detuning. The dashed green line is located at the energy of the heavy-hole exciton transitions in the HARCQW. Insets are the corresponding dark-field microscopy images, which display different colors based on the intensity ratio between UPB and LPB.

(B) Normalized 2D scattering spectra map with different levels of detuning between the heavy-hole exciton energy and the plasmon resonance. The dashed white line indicates the heavy-hole exciton transition energy.

(C) Dispersions of the exciton-plasmon polariton states as a function of the detuning. The blue squares (peak energy of the upper polariton branch [UPB]) and the red circles (peak energy of the lower polariton branch [LPB]) are experimental data. The blue (UPB) and red (LPB) solid lines are the computational results using the coupled harmonic oscillator model. The dashed black line indicates the heavy-hole exciton transition energy, and the dashed green line indicates the uncoupled LSP energy.

(D) Coupling strength (red circles), *g*, extracted from the experimental results for various nanocube sizes (different detuning). The dash-dot black line is a model fitting (*L*, nanocube size; $n = 1.23 \pm 0.28$), which is in good agreement with the theoretical expectation. Blue squares depict the strictest criterion of strong coupling.

(E) Comparison of the Rabi energy and cooperativity in different exciton-plasmon hybrid systems. The open stars represent organic materials, and the solid stars denote inorganic materials.

reports,[5–8,10,11,29] where $\gamma_{LSP}$ and $\gamma_{hl\text{-}ex}$ are the linewidths of the plasmon resonance and heavy-hole exciton transition, respectively. Therefore, fulfillment of our criterion guarantees the strong coupling condition between exciton and plasmon in our hybrid system. In Figure 2D, *g* is plotted as a function of the nanocube size (i.e., different detuning values); *g* is always larger than the corresponding critical value. This finding suggests that spectral splitting in our system is caused by Rabi energy exchange rather than Fano resonance or absorbance dip enhancement. We also notice that *g* varies with the nanocube size (smaller nanocubes exhibit larger *g*). This trend can be fitted by a scaling of $g \propto 1/L^n$ ($n = 1.23 \pm 0.28$), which is roughly consistent with the expected scaling, $g \propto 1/\sqrt{V} \propto 1/L$.[27,29] However, the correlation is not very strong, which is possibly due to the roughness of the HARCQW film, the variance in the number of excitons per nanocube, and the diversity of the distance between the nanocubes and the HARCQW film.

Please cite this article in press as: Yu et al., Strong Plasmon-Wannier Mott Exciton Interaction with High Aspect Ratio Colloidal Quantum Wells, Matter (2020), https://doi.org/10.1016/j.matt.2020.03.013



For active operation of plasmonic devices, besides the Rabi energy, another benchmarking parameter is cooperativity (*C*), defined as $(\hbar\Omega)^2/\gamma_{LSP}\gamma_{hl-ex}$, which quantifies the probability that an optical emitter radiates into a distinct light mode.[15,49,50] Figure 2E compares the Rabi energy and the corresponding cooperativity in different plasmon-exciton systems. Only collective Rabi energy splitting values in references are compared here. Typically, inorganic materials (e.g., Transition metal dichalcogenide and CdSe quantum dots) only exhibit small Rabi energy (<200 meV) and *C* values (<4) due to the weak oscillator strength of Wannier Mott excitons.[5–11,15–17] On the other hand, *C* values in organic materials can be as large as 9, benefiting from the intrinsic properties of Frenkel excitons.[19–29] Recently, Norris et al.[15] achieved a *C* value up to 10.5 in a CdSe CQWs-plasmon system by taking advantage of the sharp LSP resonance (linewidth, 32 meV) in electron-beam lithographically fabricated metallic photonic crystals, although the Rabi energy in their system was only 110 meV. Here, in our simple and solution-processable system, we achieved cooperativity exceeding 11 despite the broad plasmon profile (linewidth, ~ 340 meV).

### Microscopic Origin of the Strong Interaction

Let us revisit the relationship whereby the Rabi energy or coupling strength is proportional to $\sqrt{fN/V}$ to figure out the possible mechanisms that are responsible for the giant Rabi splitting observed in our silver nanocube-HARCQW system (we also analyze the coupling using low aspect ratio CQWs, which present a Rabi energy of ~160 meV, matching the values in previous reports,[15,17,37] see Figure S4 for details). The first term to consider is the exciton binding energy ($E_{bx}$) because larger exciton binding energy resulting from enhanced wavefunction overlap not only greatly suppresses the thermal ionization but also increases the oscillator strength, thus allowing for stable and strong energy exchange between excitons and plasmons.[3,5] In low aspect ratio CQWs (LARCQWs), such as square-shaped CQWs, quantum confinement is only strong along the vertical direction because the lateral sizes are much larger than the exciton Bohr radius (~5.7 nm).[38] In contrast to LARCQWs, excitons in HARCQWs are additionally confined along one lateral direction because the lateral size is significantly tailored down (see Figure 3A). As shown in the inset of Figure 3B, additional dimension in quantum confinement is expected to increase the band gap. However, the shift of excitonic transition is negligible (see the comparison of absorbance in Figure S5) with respect to the aspect ratio of CQWs. This implies a significant increase in the exciton binding energy in these HARCQWs (inset of Figure 3B). To further confirm our interpretation, we computed the exciton binding energy in 4 ML CdSe CQWs with varying lateral sizes (the energy of free electron-hole pairs were calculated by means of the 8-band $k\cdot p$ model; then, using the measured first excitonic absorption features, the exciton binding energy can be extracted; see details in Note S3).[51] Figure 3B shows that the exciton binding energy holds a negative correlation with the lateral size of the CQWs, in agreement with our previous explanation. Notably, when the lateral size is close to or beyond the Bohr radius (vertical dashed line in Figure 3B), $E_{bx}$ is enhanced by more than 50% compared with the value in square-shaped CQWs.[38,51]

Fast exciton consumption is another challenge in hybrid systems because energy exchange needs to be faster than any dissipative processes in excitons to achieve a strong interaction.[1] Self-assembling (or stacking) in CQW solid film has been problematic for exciton reservation.[39–41,46] Our group has reported that, owing to the large absorption cross-section of CQWs and their close-packed collinear orientation in a stacked CQW film, homo-FRET among the same material is extremely fast (<100 ps) and ultra-efficient (efficiency can reach >60% at room temperature), which can even dominate the multiexciton Auger recombination.[39] Thus, exciton transfer and trapping are rapidly boosted. The main reason for stacking[46] is that the van

Please cite this article in press as: Yu et al., Strong Plasmon-Wannier Mott Exciton Interaction with High Aspect Ratio Colloidal Quantum Wells, Matter (2020), https://doi.org/10.1016/j.matt.2020.03.013



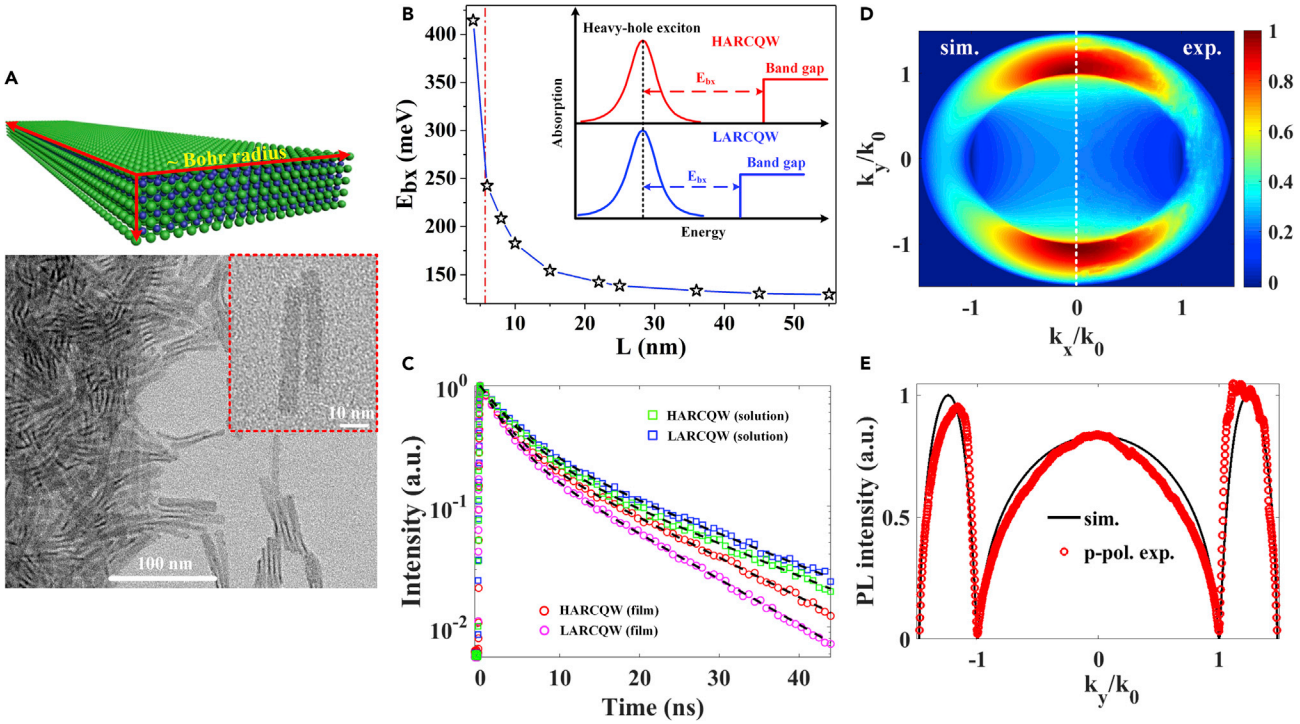


**Figure 3. Material Properties Responsible for a Giant Rabi Energy**

(A) Morphology of the HARCQWs. Top panel: schematic of the HARCQWs. Bottom panel: self-assembly of HARCQWs. The TEM image shows the random-oriented, non-stacking, and face-down assembly. The inset in the bottom panel: TEM image of an individual HARCQW; the lateral size is about ~50 nm by 5–8 nm.

(B) The exciton binding energy as a function of the lateral size in 4 ML CdSe CQWs. The solid line is a guide to the eye. The dashed black line indicates the exciton Bohr radius (~5.7 nm) in bulk CdSe. Inset: impact of the aspect ratio on the exciton binding energy. A high aspect ratio is expected to enhance the exciton binding energy, indicated by the horizontal dashed line. The vertical dashed line shows the negligible shift of the absorbance feature with respect to the aspect ratio.

(C) Time-resolved PL decay curves (squares: in hexane; circles: in film) of the HARCQWs and LARCQWs. Black dashed lines are the multiexponential fits.

(D) Experimental and simulated k-space image of the HARCQW film. Left: calculated results for pure in-plane dipole orientation. Right: experimental data for our HARCQW film.

(E) Comparison between the experimental (red circles) and simulated (black line) results cutting along the line in which $k_x = 0$ ($p$ polarization) to extract the fraction of the in-plane dipole in our HARCQW film.

der Waals attraction tends to align the lateral faces of CQWs parallel to each other in long needle-like chains[40,41] (see the TEM image of stacked LARCQWs in Figure S6). If we approximate the CQW as an ideal flat plate, we can express the attraction energy for stacking[46] as follows: $E_{attraction} = HA_{eff}/12\pi D^2$, where $H$ is the Hamaker constant, $D$ is the distance between the CQWs, and $A_{eff}$ is the effective interaction area. If the attraction energy is larger than $kT$ (the thermal energy), the CQW film will prefer to be stacked. Thus, the unstacking criterion can be given by $D > \sqrt{HA_{eff}/12\pi kT}$, which implies that the distance should be larger than a certain value to avoid stacking. By using the Hamaker constant from a previous report,[46] the minimum distance for LARCQWs with a square shape (18 × 18 nm) is ~7.1 nm by assuming the whole surface area is effective. This distance is larger than the length of two oleic acid ligands (4–6 nm)[34,46] and explains why LARCQWs are easy to stack. However, for HARCQWs, $A_{eff}$ can be quite small considering any small tilting or offset significantly changes the effective interaction area. If the minimum distance is reduced to be smaller than the length of two oleic acid ligands, the CQW film will not be stacked anymore. There is no doubt that HARCQWs satisfy this criterion; as shown in Figure 3A, random-oriented CQWs are lying flat on the TEM grid and there is no

Please cite this article in press as: Yu et al., Strong Plasmon-Wannier Mott Exciton Interaction with High Aspect Ratio Colloidal Quantum Wells, Matter (2020), https://doi.org/10.1016/j.matt.2020.03.013



indication of stacking. To further support our argument, we have checked the time-resolved photoluminescence (PL) of CQWs in a solution dispersion and a solid film (see Figure 3C). Both low and high aspect ratio CQWs in solution display a similar decay behavior with an average lifetime of ~3.2 ns (see Table S1 for the tri-exponential lifetime fitting). On the other hand, in solid film, for LARCQWs, the average lifetime accelerates to ~1.4 ns, indicating a strong exciton trapping via the homo-FRET process caused by stacking.[39] However, the homo-FRET process is greatly suppressed in a HARCQW film with a prolonged average lifetime of ~2.5 ns, suggesting the induced non-radiative channel is weakened.

Beyond the intrinsic properties of HARCQWs, one more point needed to be considered in our hybrid system: the effective dipole numbers, $N_{eff}$. As discussed in Figure 1, in the solid film, the total number of dipoles ($N$) is enough to ensure that they can cover the whole penetration depth of LSP. Indeed, the coupling strength ($g$) depends on the orientation of transition dipoles with respect to the electric field of the LSP mode. For a single dipole: $g_i \propto \sqrt{\cos^2(\theta_i) \times f/V}$, where $\theta_i$ denotes the angle between the dipole momentum and the electric field.[12,13,25] Thus, Rabi energy is proportional to the square root of effective dipole numbers ($N_{eff} = \sum_{i=1}^{N} \cos^2(\theta_i)$) rather than the total dipole number ($N$). In our system, the electric field of plasmon mode sustained in a silver nanocube is mainly confined in the $XY$ plane (in-plane) and oscillating along the nanocube edge[7] as seen in Figure 1D. Therefore, in-plane dipoles can maximize $\cos^2(\theta)$ and achieve a lager Rabi energy, and the vertically stacked CQWs suppress $N_{eff}$ to the minimum. Dipole orientation in CdSe CQWs has been systematically studied recently,[41,52,53] demonstrating that the fraction of in-plane dipole is close to unity (>95%) if the CQWs in the film are laid face down. Instead of using non-polar solvent to change the interfacial energy and lay down the LARCQWs as in their works, here, HARCQWs are naturally face down in the film (see the bottom panel of Figure 3A), benefiting from the non-stacking properties. This is understandable because the formation of the edge-up assembly (as opposed to face down) is because the stacking allows enough supporting area to make the CQWs stand up (the edge thickness of CQWs is only 1.2 nm). To double check the face-down assembly in our HARCQW film, we followed Gao and Scott's works to use back focal plane (BFP) images to determine the dipole orientation[41,52] (see the details of the BFP image setup and simulation in Note S4). Figure 3D shows the calculated intensity pattern for the pure in-plane dipole orientation and an experimental BFP images for our HARCQW film, which shows the mirror relationship between the simulation and the experiment, suggesting a high fraction of in-plane dipoles in the HARCQW film. To extract the fraction of in-plane dipoles, we compared the experimental and simulated curves along $k_x = 0$ (p polarization). The two dips ($k_y = \pm k_0$) in the experimental data are found to approach 0, and we can calculate that the fraction of in-plane dipoles is ~95%. In contrast to heavy-hole excitons, dipole orientations of light-hole excitons are randomly distributed. Therefore, in our work, it is difficult to observe light-hole exciton-plasmon coupling due to dipole orientation mismatch with the plasmonic modes.[41]

## The Emissive Polaritons

In view of the strong interaction between exciton and plasmon in our hybrid system, it is natural to expect to observe splitting in PL as in previous reports of exciton-photon strong coupling systems.[54,55] The PL signal from our hybrid system at room temperature is shown in Figure 4 (see the optical measurement in Experimental Procedures). The corresponding dark-field scattering spectrum (detuning,

Please cite this article in press as: Yu et al., Strong Plasmon-Wannier Mott Exciton Interaction with High Aspect Ratio Colloidal Quantum Wells, Matter (2020), https://doi.org/10.1016/j.matt.2020.03.013



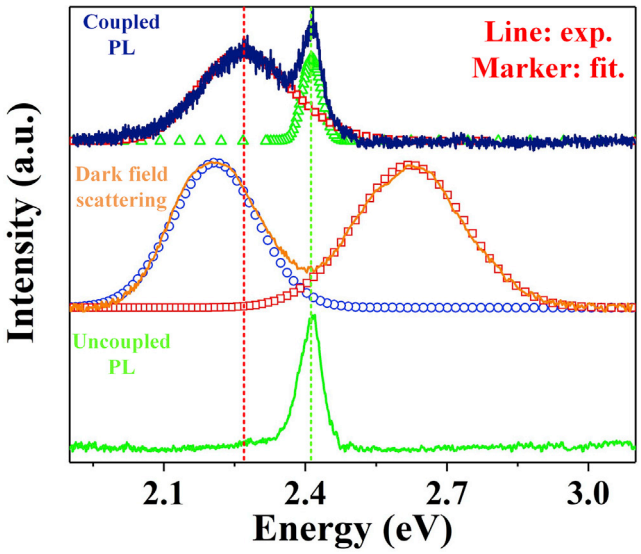


**Figure 4. PL Spectra of the Coupled Hybrid System at Room Temperature**

In the top spectrum, the narrow emission located at the high energy side is attributed to the uncoupled band-edge exciton emission. The broad emission peaking at the low energy side originates from the lower polariton states. For comparison, the dark-field scattering spectrum (the middle spectrum) with a detuning energy of 4 meV and the uncoupled PL spectrum of HARCQWs (the bottom spectrum) are also presented. The vertical green dashed line indicates the heavy-hole exciton transition at 2.42 eV. The vertical red dashed line illustrates that the emissive polariton spectrum is blue-shifted compared to the LPB in scattering measurement.

~4 meV) and PL of uncoupled HARCQW film are also presented. To rule out the possibility that the collected emission is coming from the radiative recombination between the electron in the *sp* conduction band and the hole in the *d* valence band of the Ag nanocube under lasing excitation, we checked the emission spectra of bare silver nanocubes on top of $SiO_2$/Si substrate. The result is shown in Figure S7. Under laser excitation, our sparsely distributed silver nanocube did not exhibit any noticeable emission and only background noise is collected.

Therefore, we can assign the clearly observed broad emission into the LPB emission, and the narrow emission is resulting from uncoupled band-edge excitons (located at 2.42 eV). This uncoupled emission is expected because the silver nanocube distribution is sparse, and the laser focus spot is much larger than the nanocube size.[15,54,56] Notably, the LPB emission spectrum (peaking at ~2.27 eV) is blue-shifted with respect to the corresponding LPB scattering spectrum (~2.21 eV). The reason for the higher energy LPB peak in the PL compared with the scattering is not totally understood. Our speculation for this observation is related to a "polariton bottleneck" and the contribution of dark polariton states. The former implies that the PL emission originates from not fully relaxed lower polariton states. When the pump fluence is high, the strong scattering among polariton states in LPB will accelerate the decoupling process (photons will be emitted before polariton states can relax to the bottom of LPB), which is similar to the "polariton bottleneck" observed in exciton-photon polariton systems.[55] The latter associates with $N$ excitons coupled to the plasmon to generate two bright hybrid states (LPB and UPB) and ($N - 1$) dark polariton states. Although these dark polariton states absorb weakly, they may contribute to the high energy part of the LPB emission when exciton density is high.[57,58]

Please cite this article in press as: Yu et al., Strong Plasmon-Wannier Mott Exciton Interaction with High Aspect Ratio Colloidal Quantum Wells, Matter (2020), https://doi.org/10.1016/j.matt.2020.03.013



## DISCUSSION

In summary, we have demonstrated ultra-strong interactions between excitons in CdSe HARCQWs and localized plasmon resonance in silver nanocubes. The observed value of collective Rabi splitting is up to 402 meV, which is the highest value ever achieved for Wannier excitons, and corresponds to the largest cooperativity (>11) ever reported in an open cavity exciton-polariton system. Importantly, the strong exciton-plasmon coupling is observed in both dark-field scattering and photoluminescence measurements, unambiguously suggesting the strong intermixing of excitons with plasmons to create polaritons. The main mechanisms responsible for these observations are the enhanced oscillation strength and improved in-plane exciton dipole orientation in HARCQWs. This exciton-plasmon hybrid system, based on fully solution-processable quantum emitters and metal nanostructures, may provide a feasible recipe for active all-optical nanocircuits and devices.

## EXPERIMENTAL PROCEDURES

### Synthesis of High Aspect Ratio CdSe CQWs

CdSe CQWs were synthesized by following the recipe reported previously with a few modifications.[35,59] Briefly, we began with 340 mg of cadmium myristate, 24 mg of selenium, and 30 mL of 1-octadecene in a 100 mL flask. While degassing, the temperature of the solution was slowly increased up to 95°C and then kept at this temperature for 30 min to evaporate extra solvents and dissolve myristate completely. We then raised the temperature to 245°C and placed the solution under argon at 100°C. At approximately 195°C when the color of solution became bright yellow, we introduced 120 mg of cadmium acetate with different amounts of hydrate in the crude reaction solution. This variation in hydrate content resulted in a different aspect ratio for the CQWs. The variation of the hydrate content in cadmium acetate was obtained by using different ratios of cadmium acetate anhydrous/cadmium acetate dihydrate ($Cd(OAc)_2$/$Cd(OAc)_2.2H_2O$).[59] Thereafter, we kept the solution at 240°C for 8–10 min. The reaction was completed by the addition of 1 mL of oleic acid to the solution followed by cooling the crude reaction solution to room temperature using a water bath. Using size-selective precipitation, the pure 4 ML CdSe CQW populations were separated from the crude reaction solution. The cleaning procedure was followed exactly as reported previously.[35] Finally, the precipitated sample was dissolved in hexane and used for different characterizations and applications.

### Characterization of High Aspect Ratio CdSe CQWs

Absorption spectra of HARCQWs in hexane were measured using an ultraviolet-visible spectrophotometer (Shimadzu, UV-1800). The PL spectra of HARCQWs in hexane were recorded using a spectrofluorophotometer (Shimadzu, RF-5301PC). The QY of HARCQWs in hexane (100 mg/mL) was measured with an integrating sphere and calculated as the ratio of emitted photons and absorption photons. The accuracy of the QY measurement was verified using Rhodamine 6G; the measured QY of 94.3% in our setup is in good agreement with the standard value of 95%.

### Dark-Field Scattering Spectroscopy

Dark-field scattering experiments were conducted based on a 100× objective lens (NA = 0.95) and a xenon light source (Thorlabs). Scattered photons were collected by the same objective lens and directed into a hyperspectral system (Cytoviva) for spectral analysis. A background spectrum taken from a nearby area was subtracted from each measured silver nanocube spectrum.

### Time-Resolved PL Measurement

Time-resolved PL spectroscopy was performed with a Becker & Hickl DCS 120 confocal scanning FLIM system with the laser pulse at 375 nm and a repetition rate of 20 MHz. The collection time was 180 s for all the time-resolved PL measurements.

### PL Measurement of the Hybrid System

All measurements were conducted using a frequency tripling of Nd:YAG laser (355 nm) with a pulse width of 0.5 ns at a repetition rate of 100 Hz. The sample was mounted on a three-dimensional moving stage. The laser beam was focused onto the hybrid system using a long working distance objective lens (ZEISS; NA, 0.65, 63×). The emission signal was collected using the same objective lens with a long pass filter (>450 nm).

## DATA AVAILABILITY

All experimental data are available upon reasonable request to the corresponding authors.

## SUPPLEMENTAL INFORMATION

Supplemental Information can be found online at https://doi.org/10.1016/j.matt.2020.03.013.

## ACKNOWLEDGMENTS

We would like to thank Singapore Ministry of Education for financial support through AcRF Tier1 grant (MOE2017-T1-002-142) and Singapore National Research Foundation under the Program of NRF-NEFI-2016-08. H.V.D. is grateful for additional financial support from the TUBA. M.D.B. and H.W. are grateful for financial support from the Ministry of Education through AcRF Tier 2 grant (MOE2016-T2-1-052). The W.F. is also grateful for financial support from the Singapore National Research Foundation under the Program of NRF-CRP19-2017-01.

## AUTHOR CONTRIBUTIONS

C.D. and H.V.D. led and supervised all aspects of the research. J.Y. and C.D. initiated the idea. M.D.B. initiated and supervised the polariton analysis/calculations. J.Y., H.V.D., and C.D. wrote the manuscript; S.H and L.Y.M.T. conducted the dark-field scattering measurements; M.S. performed the high aspect ratio CdSe CQWs synthesis and optimized them to achieve the best performance. S.D. helped with material synthesis and characterizations. Z.S. and W.F. performed the 8-band k●p calculations. S.H. and C.H. conducted the SEM measurements. J.Y. conducted the lifetime and BFP measurements and did the polariton calculations. H.W. and D.Z. discussed the results and provided technical advice. All authors analyzed the data, discussed the results, commented on the manuscript and participated in manuscript revision.

## DECLARATION OF INTERESTS

The authors declare no competing interests.

Received: August 22, 2019
Revised: November 7, 2019
Accepted: March 12, 2020
Published: April 14, 2020

## REFERENCES


1. Vasa, P., Wang, W., Pomraenke, R., Lammers, M., Maiuri, M., Manzoni, C., Cerullo, G., and Lienau, C. (2013). Real-time observation of ultrafast rabi oscillations between excitons and plasmons in metal nanostructures with J-aggregates. Nat. Photon. *7*, 128–132.
2. Berini, P., and De Leon, I. (2012). Surface plasmon–polariton amplifiers and lasers. Nat. Photon. *6*, 16–24.
3. Barnes, W.L., Dereux, A., and Ebbesen, T.W. (2003). Surface plasmon subwavelength optics. Nature *424*, 824–830.
4. Gramotnev, D.K., and Bozhevolnyi, S.I. (2010). Plasmonics beyond the diffraction limit. Nat. Photon. *4*, 83–91.
5. Wen, J., Wang, H., Wang, W., Deng, Z., Zhuang, C., Zhang, Y., Liu, F., She, J., Chen, J., Chen, H., et al. (2017). Room temperature strong light–matter interaction with active control in single plasmonic nanorod coupled with two-dimensional atomic crystals. Nano Lett. *17*, 4689–4697.
6. Sun, J., Hu, H., Zheng, D., Zhang, D., Deng, Q., Zhang, S., and Xu, H. (2018). Light-emitting plexciton: exploiting plasmon-exciton interaction in the intermediate coupling regime. ACS Nano *12*, 10393–10402.
7. Han, X., Wang, K., Xing, X., Wang, M., and Lu, P. (2018). Rabi splitting in a plasmonic nanocavity coupled to a $WS_2$ monolayer at room temperature. ACS Photon. *5*, 3970–3976.
8. Cuadra, J., Baranov, D.G., Wersall, M., Verre, R., Antosiewicz, T.J., and Shegai, T. (2018). Observation of tunable charged exciton polaritons in hybrid monolayer WS2-plasmonic nanoantenna system. Nano Lett. *18*, 1777–1785.
9. Stührenberg, M., Munkhbat, B., Baranov, D.G., Cuadra, J., Yankovich, A.B., Antosiewicz, T.J., Olsson, E., and Shegai, T. (2018). Strong light-matter coupling between plasmons in individual gold Bi-pyramids and excitons in mono- and multilayer $WSe_2$. Nano Lett. *18*, 5938–5945.
10. Zheng, D., Zhang, S., Deng, Q., Kang, M., Nordlander, P., and Xu, H. (2017). Manipulating coherent plasmon-exciton interaction in a single silver nanorod on monolayer $WSe_2$. Nano Lett. *17*, 3809–3814.
11. Savasta, S., Saija, R., Ridolfo, A., Di Stefano, O., Denti, P., and Borghese, F. (2010). Nanopolaritons: vacuum rabi splitting with a single quantum dot in the center of a dimer nanoantenna. ACS Nano *4*, 6369–6376.
12. Peng, P., Liu, Y.-C., Xu, D., Cao, Q.-T., Lu, G., Gong, Q., and Xiao, Y.-F. (2017). Enhancing coherent light-matter interactions through micro cavity-engineered plasmonic resonances. Phys. Rev. Lett. *119*, 233901.
13. Li, R.-Q., Hernangómez-Perez, D., García-Vidal, F.J., and Fernandez-Domínguez, A.I. (2016). Transformation optics approach to plasmon-exciton strong coupling in nanocavities. Phys. Rev. Lett. *117*, 107401.
14. Vahala, K.J. (2003). Optical microcavities. Nature *424*, 839–846.
15. Winkler, J.M., Rabouw, F.T., Rossinelli, A.A., Jayanti, S.V., McPeak, K.M., Kim, D.K., le Feber, B., Prins, F., and Norris, D.J. (2019). Room temperature strong coupling of CdSe nanoplatelets and plasmonic hole arrays. Nano Lett. *19*, 108–115.
16. Gomez, D.E., Vernon, K.C., Mulvaney, P., and Davis, T.J. (2009). Surface plasmon mediated strong exciton–photon coupling in semiconductor nanocrystals. Nano Lett. *10*, 274–278.
17. Wang, H., Wang, H.-Y., Toma, A., Yano, T.-a., Chen, Q.-D., Xu, H.-L., Sun, H.-B., and Proietti Zaccaria, R. (2016). Dynamics of strong coupling between CdSe quantum dots and surface plasmon polaritons in subwavelength hole array. J. Phys. Chem. Lett. *7*, 4648–4654.
18. Bisht, A., Cuadra, J., Wersall, M., Canales, A., Antosiewicz, T.J., and Shegai, T. (2018). Collective strong light-matter coupling in hierarchical microcavity-plasmon-exciton systems. Nano Lett. *19*, 189–196.
19. Melnikau, D., Esteban, R., Savateeva, D., Sanchez-Iglesias, A., Grzelczak, M., Schmidt, M.K., Liz-Marzan, L.M., Aizpurua, J., and Rakovich, Y.P. (2016). Rabi splitting in photoluminescence spectra of hybrid systems of gold nanorods and J-aggregates. J. Phys. Chem. Lett. *7*, 354–362.
20. DeLacy, B.G., Miller, O.D., Hsu, C.W., Zander, Z., Lacey, S., Yagloski, R., Fountain, A.W., Valdes, E., Anquillare, E., Soljacič, M., et al. (2015). Coherent plasmon-exciton coupling in silver platelet-J-aggregate nanocomposites. Nano Lett. *15*, 2588–2593.
21. Wang, H., Wang, H.-Y., Bozzola, A., Toma, A., Panaro, S., Raja, W., Alabastri, A., Wang, L., Chen, Q.-D., Xu, H.-L., et al. (2016). Dynamics of strong coupling between J-aggregates and surface plasmon polaritons in subwavelength hole arrays. Adv. Funct. Mater. *26*, 6198–6205.
22. Sugawara, Y., Kelf, T.A., Baumberg, J.J., Abdelsalam, M.E., and Bartlett, P.N. (2006). Strong coupling between localized plasmons and organic excitons in metal nanovoids. Phys. Rev. Lett. *97*, 266808.
23. Zheng, Y.B., Juluri, B.K., Lin Jensen, L., Ahmed, D., Lu, M., Jensen, L., and Huang, T.J. (2010). Dynamic tuning of plasmon–exciton coupling in arrays of nanodisk–J-aggregate complexes. Adv. Mater. *22*, 3603–3607.
24. Hao, Y.-W., Wang, H.-Y., Jiang, Y., Chen, Q.-D., Ueno, K., Wang, W.-Q., Misawa, H., and Sun, H.-B. (2011). Hybrid-state dynamics of gold nanorods/dye J-aggregates under strong coupling. Angew. Chem. Int. Ed. *50*, 7824–7828.
25. Wersall, M., Cuadra, J., Antosiewicz, T.J., Balci, S., and Shegai, T. (2017). Observation of mode splitting in photoluminescence of individual plasmonic nanoparticles strongly coupled to molecular excitons. Nano Lett. *17*, 551–558.
26. Zengin, G., Wersall, M., Nilsson, S., Antosiewicz, T.J., Kall, M., and Shegai, T. (2015). Realizing strong light-matter interactions between single-nanoparticle plasmons and molecular excitons at ambient conditions. Phys. Rev. Lett. *114*, 157401.
27. Roller, E.-M., Argyropoulos, C., Högele, A., Liedl, T., and Pilo-Pais, M. (2016). Plasmon-exciton coupling using DNA templates. Nano Lett. *16*, 5962–5966.
28. Schlather, A.E., Large, N., Urban, A.S., Nordlander, P., and Halas, N.J. (2013). Near-field mediated plexcitonic coupling and giant rabi splitting in individual metallic dimers. Nano Lett. *13*, 3281–3286.
29. Liu, R., Zhou, Z.-K., Yu, Y.-C., Zhang, T., Wang, H., Liu, G., Wei, Y., Chen, H., and Wang, X.-H. (2017). Strong light-matter interactions in single open plasmonic nanocavities at the quantum optics limit. Phys. Rev. Lett. *118*, 237401.
30. Daskalakis, K.S., Maier, S.A., Murray, R., and Kena-Cohen, S. (2014). Nonlinear interactions in an organic polariton condensate. Nat. Mater. *13*, 271–278.
31. Yin, Y.D., and Alivisatos, A.P. (2005). Colloidal nanocrystal synthesis and the organic-inorganic interface. Nature *437*, 664–670.
32. Shirasaki, Y., Supran, G.J., Bawendi, M.G., and Bulovic, V. (2012). Emergence of colloidal quantum-dot light-emitting technologies. Nat. Photon. *7*, 13–23.
33. Dang, C., Lee, J., Breen, C., Steckel, J.S., Coe-Sullivan, S., and Nurmikko, A. (2012). Red, green and blue lasing enabled by single-exciton gain in colloidal quantum dot films. Nat. Nanotechnol. *7*, 335–339.
34. Ithurria, S., Tessier, M.D., Mahler, B., Lobo, R.P.S.M., Dubertret, B., and Efros, A.L. (2011). Colloidal nanoplatelets with two dimensional electronic structure. Nat. Mater. *10*, 936–941.
35. Dede, D., Gungor, K., and Demir, H.V. (2019). Highly stable multicrown heterostructures of type-II nanoplatelets for ultralow threshold optical gain. Chem. Mater. *31*, 1818–1826.
36. Achtstein, A.W., Schliwa, A., Prudnikau, A., Hardzei, M., Artemyev, M.V., Thomsen, C., and Woggon, U. (2012). Electronic structure and exciton-phonon interaction in two-dimensional colloidal CdSe nanosheets. Nano Lett. *12*, 3151–3157.
37. Zhou, N., Yuan, M., Gao, Y., Li, D., and Yang, D. (2016). Silver nanoshell plasmonically controlled emission of semiconductor quantum dots in the strong coupling regime. ACS Nano *10*, 4154–4163.
38. Norris, D.J., Efros, A.L., Rosen, M., and Bawendi, M.G. (1996). Size dependence of exciton fine structure in CdSe quantum dots. Phys. Rev. B *53*, 16347–16354.
39. Guzelturk, B., Erden, O., Olutas, M., Kelestemur, Y., and Demir, H.V. (2014). Stacking in colloidal nanoplatelets: tuning excitonic properties. ACS Nano *8*, 12524–12533.
40. Abecassis, B., Tessier, M.D., Davidson, P., and Dubertret, B. (2014). Self-assembly of CdSe nanoplatelets into giant micrometer-scale needles emitting polarized light. Nano Lett. *14*, 710–715.
41. Scott, R., Heckmann, J., Prudnikau, A.V., Antanovich, A., Mikhailov, A., Owschimikow,

N., Artemyev, M., Climente, J.I., Woggon, U., Grosse, N.B., and Achtstein, A.W. (2017). Directed emission of CdSe nanoplatelets originating from strongly anisotropic 2D electronic structure. Nat. Nanotechnol. *12*, 1155–1160.

42. Hung, L., Lee, S.Y., McGovern, O., Rabin, O., and Mayergoyz, I. (2013). Calculation and measurement of radiation corrections for plasmon resonances in nanoparticles. Phys. Rev. B *88*, 075424.

43. Lassiter, J.B., McGuire, F., Mock, J.J., Ciracì, C., Hill, R.T., Wiley, B.J., Chilkoti, A., and Smith, D.R. (2013). Plasmonic waveguide modes of film-coupled metallic nanocubes. Nano Lett. *13*, 5866–5872.

44. Eizner, E., Avayu, O., Ditcovski, R., and Ellenbogen, T. (2015). Aluminum nanoantenna complexes for strong coupling between excitons and localized surface plasmons. Nano Lett. *15*, 6215–6221.

45. nanoComposix. Cube nanoparticles. https://nanocomposix.com/collections/shape-cubes/material-silver.

46. Jana, S., Phan, T.N.T., Bouet, C., Tessier, M.D., Davidson, P., Dubertret, B., and Abecassis, B. (2015). Stacking and colloidal stability of CdSe nanoplatelets. Langmuir *31*, 10532–10539.

47. Santhosh, K., Bitton, O., Chuntonov, L., and Haran, G. (2016). Vacuum Rabi splitting in a plasmonic cavity at the single quantum emitter limit. Nat. Commun. *7*, 11823.

48. Gao, W., Li, X., Bamba, M., and Kono, J. (2018). Continuous transition between weak and ultrastrong coupling through exceptional points in carbon nanotube microcavity exciton-polaritons. Nat. Photon. *12*, 362–367.

49. Stehle, C., Zimmermann, C., and Slama, S. (2014). Cooperative coupling of ultracold atoms and surface plasmons. Nat. Phys. *10*, 937–942.

50. Groß, H., Hamm, J.M., Tufarelli, T., Hess, O., and Hecht, B. (2018). Nearfield strong coupling of single quantum dots. Sci. Adv. *4*, eaar4906.

51. Bose, S., Shendre, S., Song, Z., Sharma, V.K., Zhang, D.H., Dang, C., Fan, W., and Demir, H.V. (2017). Temperature-dependent optoelectronic properties of quasi-2D colloidal cadmium selenide nanoplatelets. Nanoscale *9*, 6595–6605.

52. Gao, Y., Weidman, M.C., and Tisdale, W.A. (2017). CdSe Nanoplatelet Films with Controlled Orientation of their Transition Dipole Moment. Nano. Lett. *17*, 3837–3843.

53. Heckmann, J., Scott, R., Prudnikau, A.V., Antanovich, A., Owschimikow, N., Artemyev, M., Climente, J.I., Woggon, U., Grosse, N.B., and Achtstein, A.W. (2017). Directed two-photon absorption in CdSe nanoplatelets revealed by k-space spectroscopy. Nano Lett. *17*, 6321–6329.

54. Su, R., Diederichs, C., Wang, J., Liew, T.C., Zhao, J., Liu, S., Xu, W., Chen, Z., and Xiong, Q. (2017). Room temperature polariton lasing in all-inorganic perovskite nanoplatelets. Nano Lett. *17*, 3982–3988.

55. Bajoni, D. (2012). Polariton lasers. Hybrid light–matter lasers without inversion. J. Phys. D Appl. Phys. *45*, 4211–4216.

56. Hou, S., Tobing, L.Y., Wang, X., Xie, Z., Yu, J., Zhou, J., Zhang, D., Dang, C., Coquet, P., Tay, B.K., et al. (2019). Manipulating coherent light matter interaction: continuous transition between strong coupling and weak coupling in $MoS_2$ monolayer coupled with plasmonic nanocavities. Adv. Opt. Mater. *7*, 1900857.

57. Zhang, X., Xu, Q., Li, Q., Xu, Y., Gu, J., Tian, Z., Ouyang, C., Liu, Y., Zhang, S., Zhang, X., et al. (2016). Asymmetric excitation of surface plasmons by dark mode coupling. Sci. Adv. *2*, e1501142.

58. Herrera, F., and Spano, F.C. (2017). Dark vibronic polaritons and the spectroscopy of organic microcavities. Phys. Rev. Lett. *118*, 223601.

59. Bertrand, G.H.V., Polovitsyn, A., Christodoulou, S., Khan, A.H., and Moreels, I. (2016). Shape control of zincblende CdSe nanoplatelets. Chem. Commun. *52*, 11975–11978.

**Matter, Volume *2***

## Supplemental Information

# Strong Plasmon-Wannier Mott Exciton Interaction with High Aspect Ratio Colloidal Quantum Wells

**Junhong Yu, Songyan Hou, Manoj Sharma, Landobasa Y.M. Tobing, Zhigang Song, Savas Delikanli, Chathuranga Hettiarachchi, Daohua Zhang, Weijun Fan, Muhammad Danang Birowosuto, Hong Wang, Hilmi Volkan Demir, and Cuong Dang**

## Supplementary Figure 1

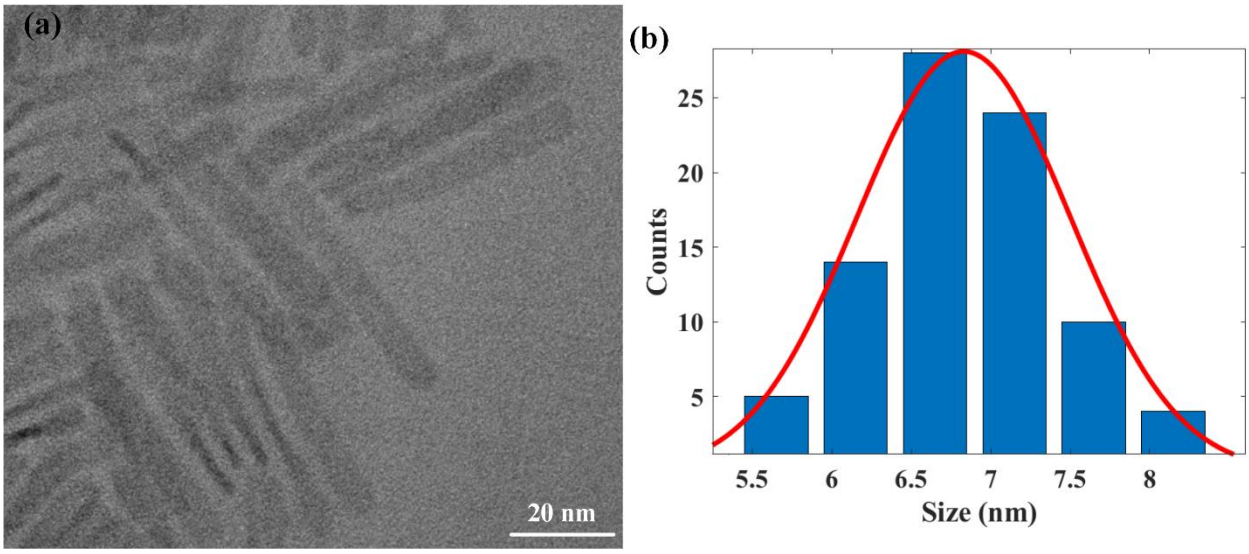


**Figure S1**. Lateral size distribution of high aspect ratio 4 ML CdSe CQWs. **(a)** TEM images, the scale bar is 20 nm. **(b)** Size histograms of the short side. Red line is the Gaussian fitting curves, indicating the short side length is in the range of 5-8 nm (Bohr radius of CdSe: ~5.7 nm).

**Supplementary Figure 2**

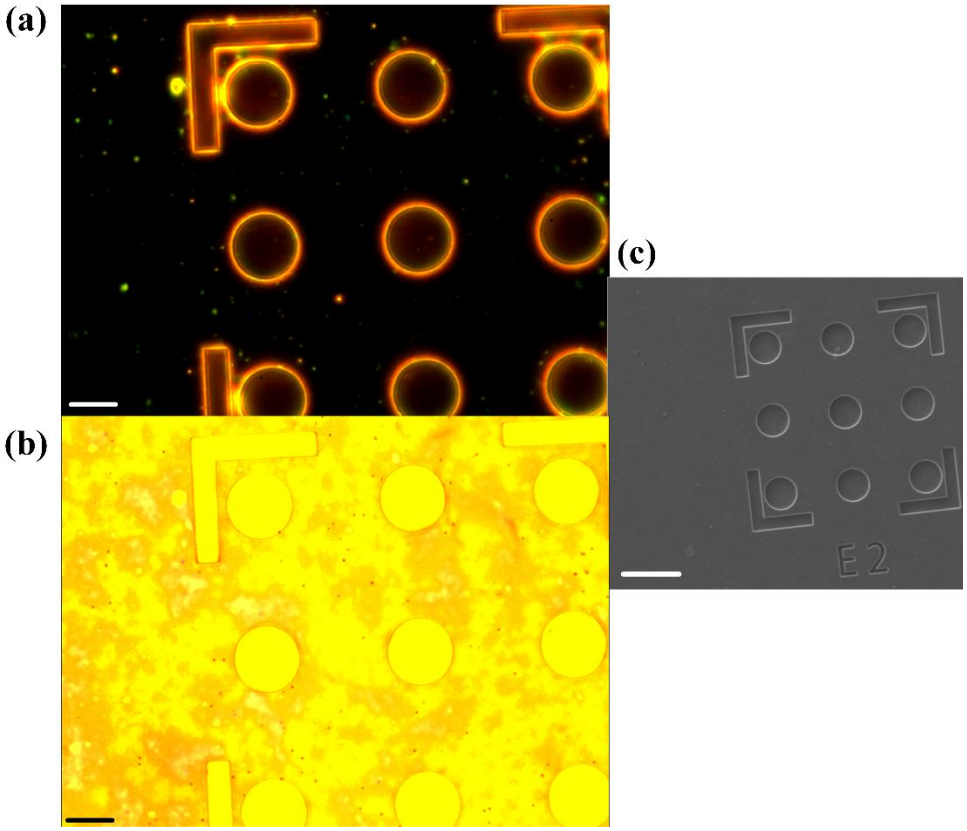


**Figure S2**. Features over the Si/SiO2 substrate as an indicator of the nanocube location. **(a)** Dark-field scattering image, the scale bar is 5 µm. **(b)** Bright-field microscopy image, the scale bar is 5 µm. **(c)** SEM image, the scale bar is 10 µm.

**Supplementary Figure 3**

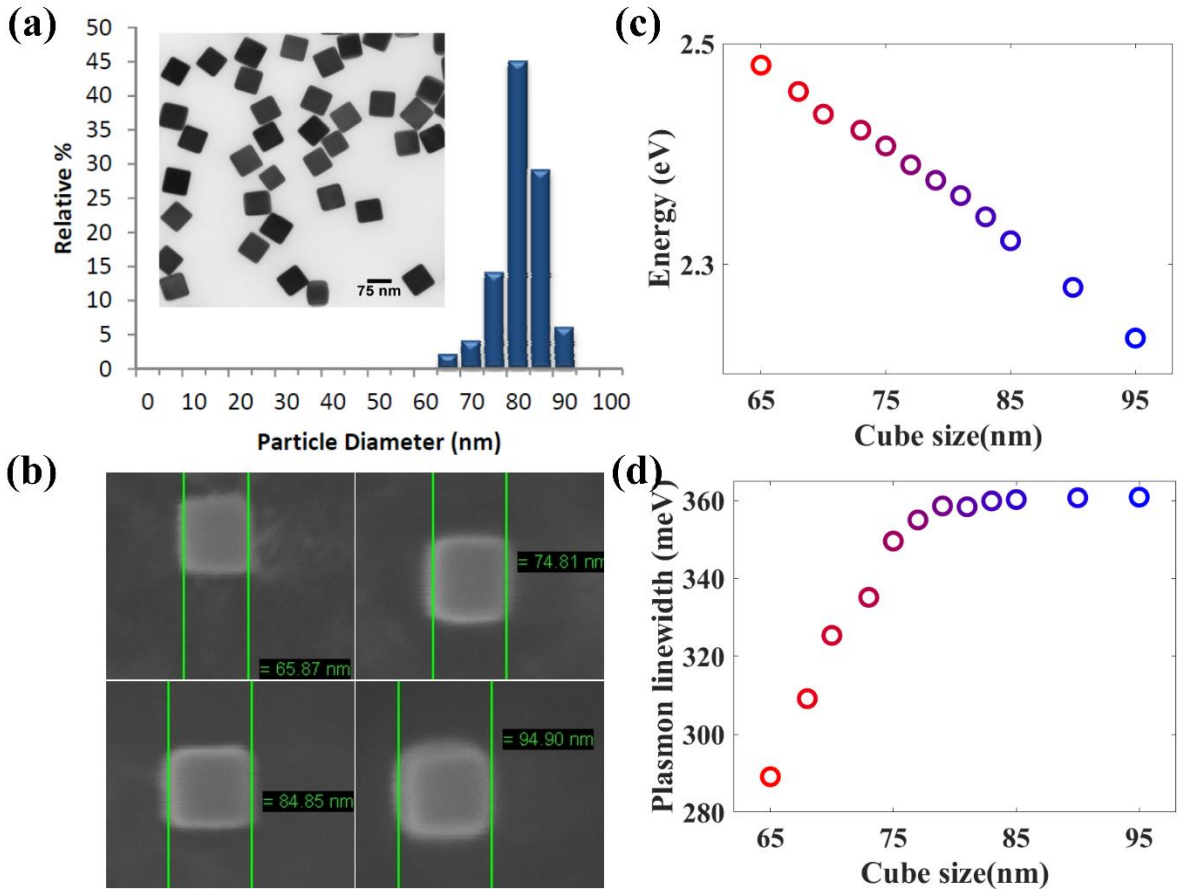


**Figure S3**. Silver nanocubes. **(a)** The size distribution of silver nanocubes. Cited from https://tools.nanocomposix.com:48/cdn/coa/Silver/Nanocubes/. The mean value is ~78 nm and the deviation is ~6.5%. **(b)** The SEM images of nanocubes on $Si/SiO_2$ substrate (using 65, 75, 85 and 95 nm as examples). The size is marked using SMILEVIEW software. **(c)** The scattering peak versus nanocube size. As the size of silver nanocube increases, the scattering peak red-shifts in the contribution of retardation effect. [1] **(d)** The linewidths change of scattering spectra. As the size of silver nanocube increases, the spectra become broader as the diluted surface charge density distribution in lager silver nanocube. [2]

## Supplementary Figure 4

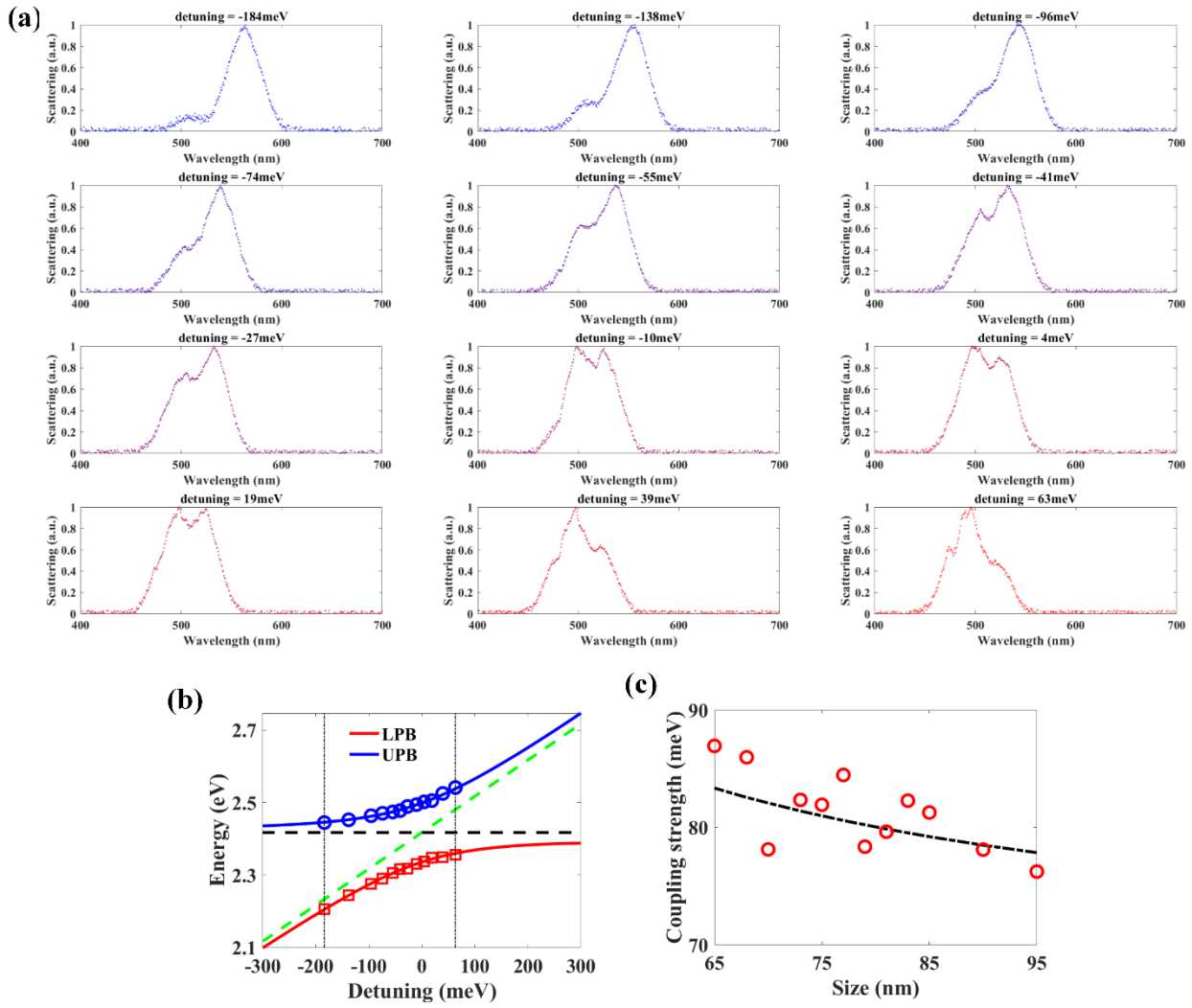


**Figure S4**. The Rabi splitting in the same hybrid system using low aspect ratio CQWs. **(a)** The dark-field scattering spectra. **(b)** Anti-crossing behavior, the calculated Rabi energy is ~162 meV. **(c)** The coupling strength as a function of nanocube size. The dashed black curve is a fitting ( $g \propto 1/L^n$ , n: ~1.17).

**Supplementary Figure 5**

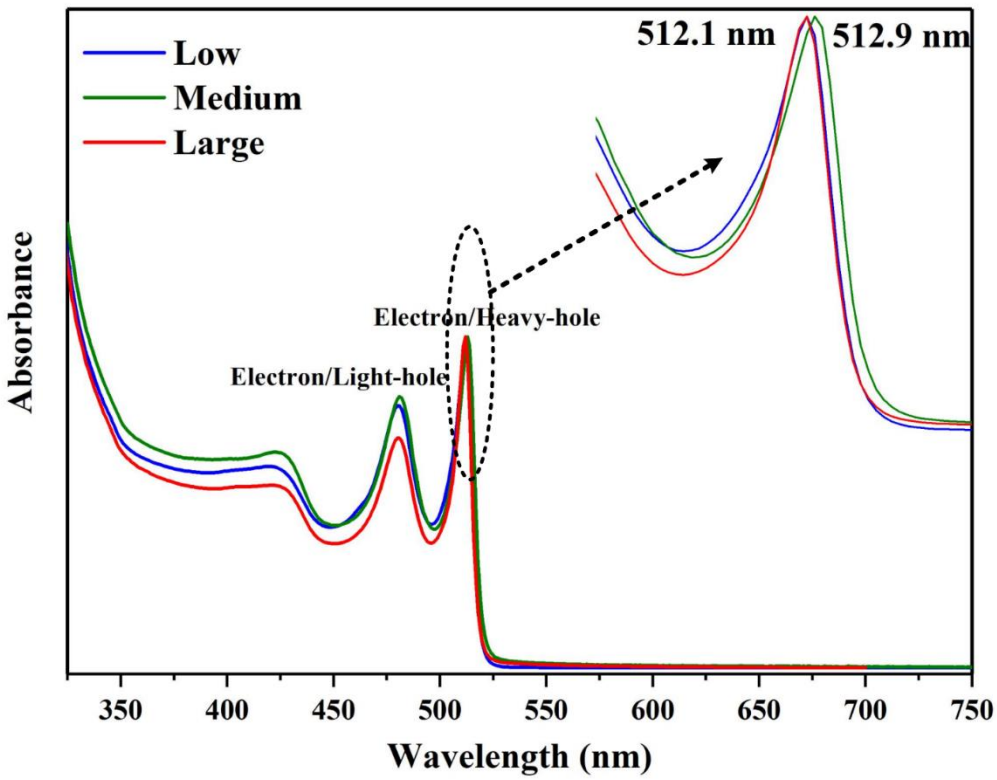


**Figure S5**. The normalized absorbance spectra of 4 ML CdSe CQWs with varying lateral size (high: ~50 × ~8 nm, medium: ~24 × ~14 nm; low: ~24 × ~22 nm). The right-top corner is the zoom-in of electron-heavy hole transition, which suggests that the energy shift of the first excitonic transition in CQWs with varing lateral size is negligible.

## Supplementary Figure 6


**Figure S6**. TEM image of stacked LARCQWs (lateral size: ~24 × ~14 nm). We can clearly see the column-like chain is formed in the LARCQW ensemble.

## Supplementary Figure 7

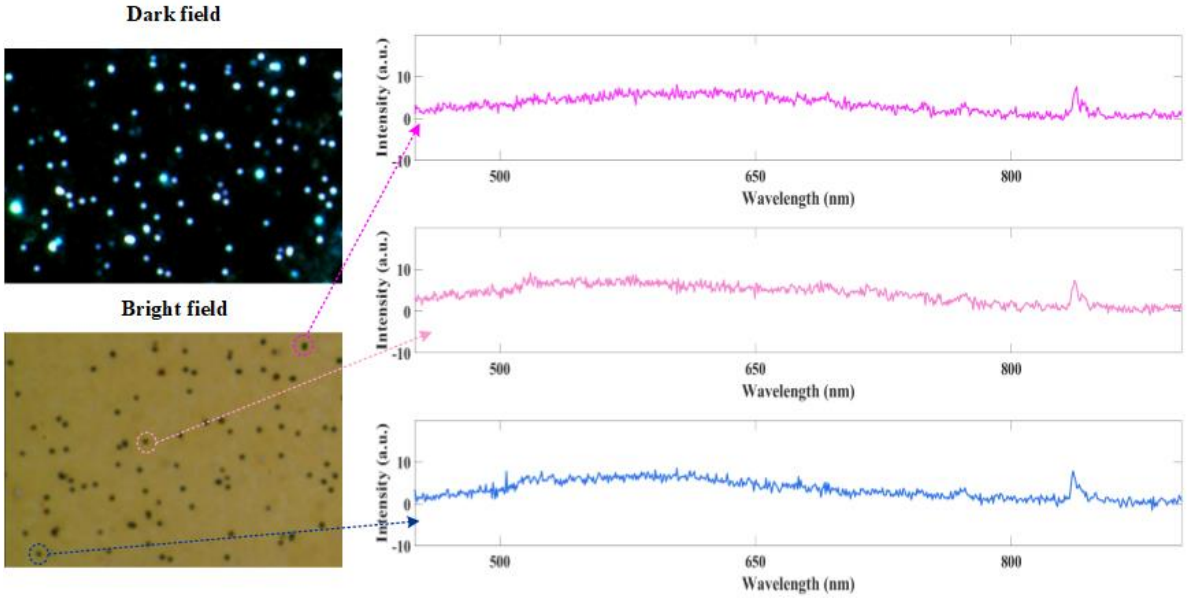


**Figure S7**. Bright filed signal in the bare silver nanocube. Spectra of three different locations are shown as representative examples. Dark field images are also presented for reference.

## Supplementary Table 1

**Table S1.** Fitting components of trPL decay for HARCQWs (in film and in hexane) and LARCQWS (in film and in hexane). The measurement is probed at the band-edge emission wavelength (electron-heavy hole transition: ~514 nm).

| | $\tau_1$ (ns) | $\tau_1$ (ns) | $\tau_1$ (ns) | $A_1$ (%) | $A_1$ (%) | $A_1$ (%) | $\tau_{avg}$ (ns) |
|---|---|---|---|---|---|---|---|
| **HARCQWs (in solution)** | 0.91 | 4.15 | 16.8 | 60.7 | 30.9 | 8.4 | 3.25 |
| **HARCQWs (film)** | 0.88 | 3.47 | 15.3 | 60.2 | 34.5 | 5.3 | 2.54 |
| **LARCQWs (in solution)** | 0.87 | 4.05 | 16.3 | 55.3 | 36.9 | 7.8 | 3.26 |
| **LARCQWs (film)** | 0.41 | 2.72 | 11.6 | 71.4 | 24.8 | 3.8 | 1.41 |

## Supplementary Note 1

Three-dimensional finite difference time domain (FDTD) simulations were performed to calculate the optical modes in plasmonic cavities. A silver nanocube is directly placed on top of CdSe CQW film. The silver nanocube is assumed to be 75 nm edge length, edge rounding of 3 nm and corner rounding of 5 nm. The silver nanocube is also coated with 3 nm polyvinylpyrrolidone (PVP) to increase the stability in the air. The silver nanocube are modeled as a dispersive Drude metal with parameters obtained by fitting tabulated data from Palik in the experimental wavelength range (from 400 nm to 600 nm). And the PVP layer is modeled as a dispersionless dielectric with a refractive index of 1.53.

The dielectric properties of CdSe CQW film is measured using an ellipsometer (VASE, J.A. Woollam, spectral range from 193 nm to 3200 nm) and the results are shown in Figure S8:

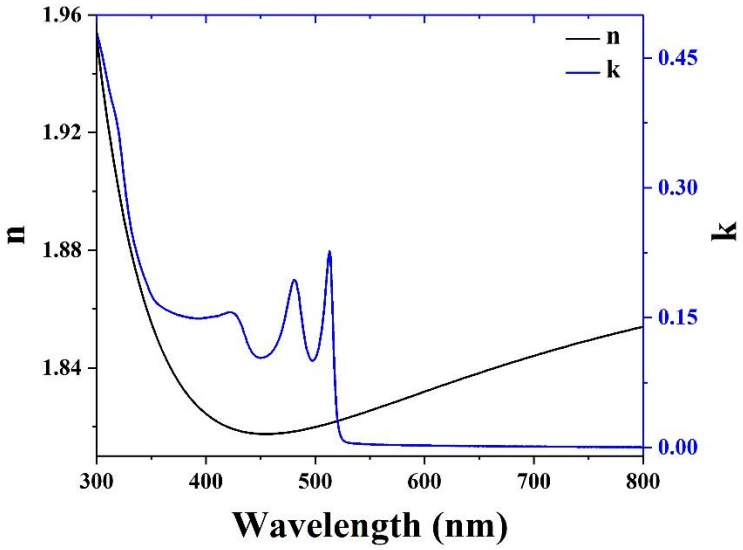


**Figure S8.** Permittivity of CdSe CQW film.

Moreover, a dielectric layer on top of CdSe CQW film with the thickness of 3 nm is inserted to consider the oleic acid ligands. The ligand layer is also modeled as a dispersionless dielectric with a refractive index of 1.45. The construct is illuminated with a plane wave (Total field scattered field source, X polarization) at the angle of $0^{\circ}$ to couple with in-plane plasmon cavity modes. The incident wavelength is swept from 400 nm to 650 nm using inbuilt sweep parameter. Three DFT-Monitors (Frequency domain power monitor) are used to obtain the electric field distributions at x-y, x-z views in Figure 1d.

## Supplementary Note 2

The exciton-photon hybrid states can be described by the coupled harmonic oscillator model:

$$\begin{vmatrix} E_{LSP} - i\frac{\gamma_{LSP}}{2} & g \\ g & E_{hl} - i\frac{\gamma_{hl}}{2} \end{vmatrix} \begin{vmatrix} \alpha \\ \beta \end{vmatrix} = E_{\mathrm{P}} \begin{vmatrix} \alpha \\ \beta \end{vmatrix} \tag{S1}$$

Where $E_{LSP}$ and $E_{hl}$ are the energy of plasmon mode and heavy-hole exciton, respectively. $g$ is the coupling strength. $\gamma_{LSP}$ and $\gamma_{hl}$ are the linewidth of plasmon mode and heavy-hole exciton, respectively. $\alpha$ and $\beta$ are Hopfield coefficients. Diagonalize this Hamiltonian and do approximation to find the two eigenvalues:

$$E_P = \frac{(\delta + 2E_{hl}) \pm \sqrt{4g^2 + \delta^2}}{2} \tag{S2}$$

Where $\delta$ is the detuning energy and defined as: $\delta = E_{LSP} - E_{hl}$ . At zero detuning, the energy difference between lower and high polariton states is the Rabi energy.

The calculated dispersion of LPB and UPB is shown in Figure 2c, which exhibits great agreement with experimental data. In addition, the extracted Hopfield coefficients of LPB and UPB are shown below:

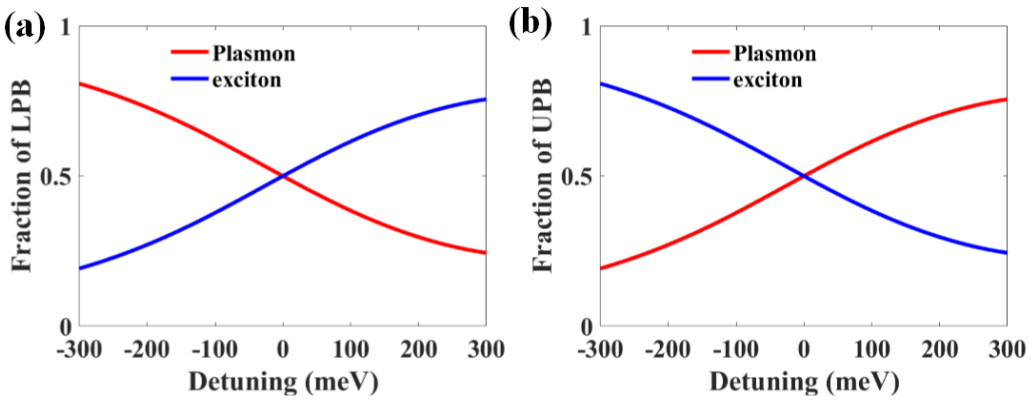


**Figure S9.** Hopfield coefficients for LPB (a) and UPB (b), calculated using the coupled harmonic oscillator model.

It can be seen that as the plasmon energy increases (larger detuning), the fraction of exciton constituent in LPB will be enhanced, while in UPB, the fraction of exciton constituent will be suppressed. Specifically, the polariton modes becomes half plasmon half exciton when the plasmon energy is matching the energy of excitonic transition in HARCQWs.

## Supplementary Note 3

The 8-band $k \bullet p$ is used to study the energy levels of free electron-hole pair in colloidal quantum wells (CQWs). Then using the measured first excitonic absorption features, we can calculate the exciton binding energy. The Hamiltonian is represented in the Bloch function basis $|S,\uparrow\rangle$ , $|S,\downarrow\rangle$ , $|11,\uparrow\rangle$ , $|10,\uparrow\rangle$ , $|1-1,\uparrow\rangle$ , $|11,\downarrow\rangle$ , $|10,\downarrow\rangle$ , $|1-1,\downarrow\rangle$ as:

$$H_8 = H_0 + V \tag{S3}$$

Where $H_0$ describes the material and the $V$ denotes the confinement of the CQWs. As we use the basis $|10\rangle$ , $|1-1\rangle$ , $|11\rangle$ for the p-like states instead of $|HH\rangle$ , $|LH\rangle$ , $|SO\rangle$ , the form of Hamiltonian is different from the traditional $JJ_z$ representation model and can be transformed into it under an unitary transformation. The details of the elements in $H_0$ is given as follows:

$$H_0 = \begin{pmatrix} E^C & 0 & iP_-^*/\sqrt{2} & iP_z & iP_+^*/\sqrt{2} & 0 & 0 & 0 \\ 0 & E^C & 0 & 0 & 0 & iP_-^*/\sqrt{2} & iP_z & iP_+^*/\sqrt{2} \\ -iP_-/\sqrt{2} & 0 & HH & S & R & 0 & 0 & 0 \\ -iP_z & 0 & S^* & Q-2\lambda & S & -\sqrt{2}\lambda & 0 & 0 \\ -iP_+/\sqrt{2} & 0 & R^* & S^* & HH-\lambda & 0 & \sqrt{2}\lambda & 0 \\ 0 & -iP_-/\sqrt{2} & 0 & -\sqrt{2}\lambda & 0 & HH-\lambda & S & R \\ 0 & -iP_z & 0 & 0 & \sqrt{2}\lambda & S^* & Q-2\lambda & S \\ 0 & -iP_+/\sqrt{2} & 0 & 0 & 0 & R^* & S^* & HH \end{pmatrix} \tag{S4}$$

where

$$\begin{aligned} &E^C = E_g + \frac{\hbar^2}{2m_0}\gamma_c(k_x^{\,2}+k_y^{\,2}+k_z^{\,2}) + \delta E_{strain}^{CB}; HH = -\frac{\hbar^2}{2m_0}[\frac{L'+M'}{2}(k_x^{\,2}+k_y^{\,2}) + M'k_z^{\,2}] + \delta E_{strain}^{HH} \\ &Q = -\frac{\hbar^2}{2m_0}[\mathrm{M}'(k_x^{\,2}+k_y^{\,2}) + L'k_z^{\,2}] + \delta E_{strain}^{Q}; S = -\frac{\hbar^2}{2m_0}[\frac{1}{\sqrt{2}}\mathrm{N}'(k_x+ik_y)k_z] + \delta E_{strain}^{S} \\ &R = -\frac{\hbar^2}{2m_0}[\frac{L'-M'}{2}(k_x^{\,2}-k_y^{\,2}) + \mathrm{iN}'k_xk_y] + \delta E_{strain}^{R}; \\ &P_- = p_0(\mathrm{k}_x'-\mathrm{ik}_y'); P_+ = p_0(\mathrm{k}_x'+\mathrm{ik}_y'); \mathrm{P}_z = p_0\,\mathrm{k}_z'; p_0 = \hbar\sqrt{E_p/2m_0} \\ &L' = L - \frac{E_p}{E_g}; \mathrm{N}' = N - \frac{E_p}{E_g}; \mathrm{M}' = M; \lambda = \Delta_{SO}/3; \gamma_c = \frac{m_0}{m_c} - \frac{E_p}{3}(\frac{2}{E_g} + \frac{1}{E_g+3\lambda}) \end{aligned} \tag{S5}$$

As in our CdSe CQWs, the strain is taken to be zeros. The confinement potential $V$ is described by the function:

$$V = \begin{cases} 0 & ,in \\ V_0 & ,out \end{cases} \tag{S6}$$

We assume that the QDs are periodically arranged in three dimensions and with the period $L_x, L_y, L_z$. We have used the plane waves to expand the basis as follows:

$$\Phi_m = \left\{ \Phi_m^j \right\} (\mathrm{j} = 1, 2, ....., 8) \tag{S7}$$

With $\Phi_m^j = \frac{1}{\sqrt{V}} \sum_{n_x, n_y, n_z} \alpha_{m, n_x, n_y, n_z}^j \exp[i(k_{nx}x + k_{ny}y + k_{nz}z)]$ . Where $V = L_x L_y L_z$ , $k_{nx} = \frac{2\pi n_x}{L_x}$ , $k_{ny} = \frac{2\pi n_y}{L_y}, k_{nz} = \frac{2\pi n_z}{L_z}$ and $n_x, n_y, n_z$ are the integer of plane wave numbers. Here we set the range of these plane wave numbers from -3 to 3. The j is the index of basis. All parameters used in calculation are listed in Table S2.

**Table S2.** All parameters used for calculation. [3]

| | **Physical parameter** | **Value** |
|---|---|---|
| $E_g$(eV) | Bandgap energy | 1.732 |
| $E_p$(eV) | kane matrix element | 16.5 |
| $\Delta_{SO}$(eV) | Spin-orbital splitting energy | 0.42 |
| $\gamma_1$ | Luttinger parameters | 3.265 |
| $\gamma_2$ | Luttinger parameters | 1.162 |
| $\gamma_3$ | Luttinger parameters | 1.443 |
| $m_c$ | Electron effective mass | 0.12 |

## Supplementary Note 4

We follow the work of Gao *et al.*[4] *and* Scott et al.[5] to simulate the back focal image of nanoparticles' emission. About the details of the Formula Derivation, we recommend readers refer to the original publication. Here, we reproduce their final version of formulas to fit our experimental results and extract the fraction of in-plane (IP) and out-plane (OP) dipoles.

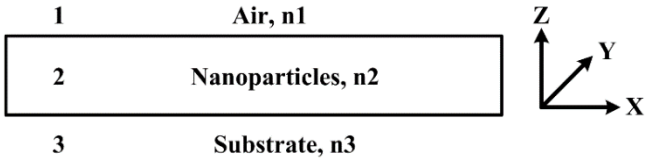


**Figure S10**. The geometry of three-layer structure

The geometry (three-layer structure) used for back focal plane imaging simulation is shown in Figure S10. Using the Fresnel equations, we can calculate the reflection and transmission coefficients of S/P polarization in the interface between two adjacent layers:

$$r_{ij}^{p}=\frac{n_j{}^2k_{zi}-n_i{}^2k_{zj}}{n_j{}^2k_{zi}+n_i{}^2k_{zj}};t_{ij}^{p}=\frac{2n_in_jk_{zi}}{n_j{}^2k_{zi}+n_i{}^2k_{zj}};$$
$$r_{ij}^{s}=\frac{2k_{zi}}{k_{zi}+k_{zj}};t_{ij}^{s}=\frac{k_{zi}-k_{zj}}{k_{zi}+k_{zj}}; \quad \text{(S8)}$$

Where $k_z$ is the wave-vector along z direction and derived based on the wave-vector conservation along X/Y direction, $n_i$ is the refractive index of $i_{th}$ layer.

$$\rho_{IP}^{S}=\frac{1}{8\pi k_0 k_{z3}}\left|\frac{t_{32}^{s}e^{\frac{ik_{z2}L}{2}}(1+\mathrm{r}_{21}^{s}e^{ik_{z2}L})}{1-\mathrm{r}_{21}^{s}\mathrm{r}_{23}^{s}e^{2ik_{z2}L}}\frac{k_y}{\sqrt{k_x^2+k_y^2}}\right|^2;$$

$$\rho_{IP}^{P}=\frac{1}{8\pi k_0 k_{z3}}\left|\frac{t_{32}^{p}e^{\frac{ik_{z2}L}{2}}\frac{k_{z2}}{n_2k_0}(1-\mathrm{r}_{21}^{p}e^{ik_{z2}L})}{1-\mathrm{r}_{21}^{p}\mathrm{r}_{23}^{p}e^{2ik_{z2}L}}\frac{k_x}{\sqrt{k_x^2+k_y^2}}\right|^2; \quad \text{(S9)}$$

$$\rho_{OP}^{P}=\frac{1}{8\pi k_0 k_{z3}}\left|\frac{t_{32}^{p}e^{\frac{ik_{z2}L}{2}}\frac{k_x}{n_2k_0}(1+\mathrm{r}_{21}^{p}e^{ik_{z2}L})}{1-\mathrm{r}_{21}^{p}\mathrm{r}_{23}^{p}e^{2ik_{z2}L}}\right|^2;$$

Based on these coefficients, we can calculate the local density of optical states (LDOS) for IP dipole and OP dipole using the above equations (here, OP dipole can only show P polarization), where $k_0$ is the wavevector in air, L is the thickness of nanoparticle layer and other symbols are denoted as mentioned before.

Thus, we can calculate the emission intensity of s- or p-polarization projected on the back focal plane with certain wave-vector ($k_x$, $k_y$) based on the population fraction ($f$) and LDOS (ρ) of IP or OP dipoles (C is an experimental determined constant):

$$I^{s}=C\rho_{IP}^{S}f_{IP}\left|\mu_{IP}\right|^2$$
$$I^{P}=C(\rho_{IP}^{P}f_{IP}\left|\mu_{IP}\right|^2+\rho_{OP}^{P}f_{OP}\left|\mu_{OP}\right|^2) \quad \text{(S10)}$$

The simulated BFP image densities for pure IP and OP transition dipoles are shown below:

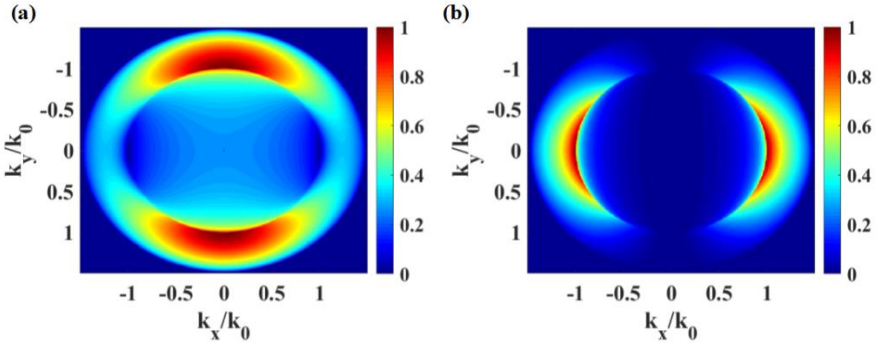


**Figure S11**. Simulated BFP image of IP (a) and OP (b) dipole transitions.

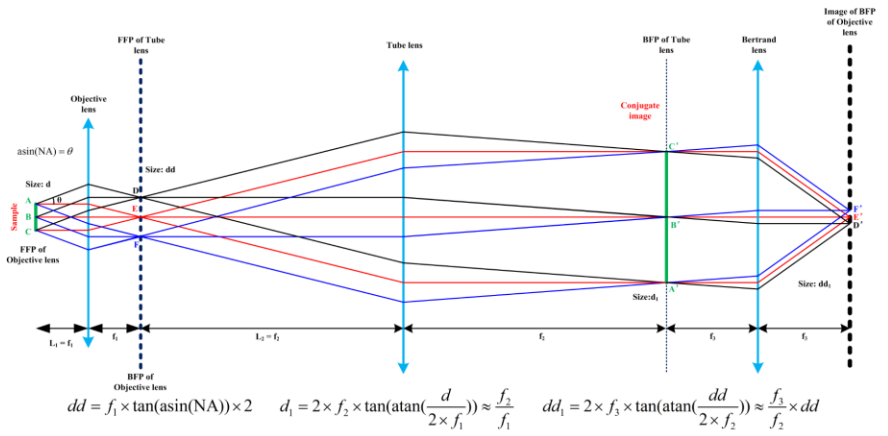


**Figure S12**. Ray tracing of the set-up to measure BFP image.

For the experimental part, the set-up used to measure the BFP image is shown in Figure S12 (excitation laser, polarizer and CCD camera are not presented). To confirm the validation of the set-up, we have utilized the strip silver grating to compare the real-space image and Fourier-space image, the result is shown in Figure S13, we can observe that in Fourier space, the horizontal stripes in real-space have been converted into vertically distributed dots.

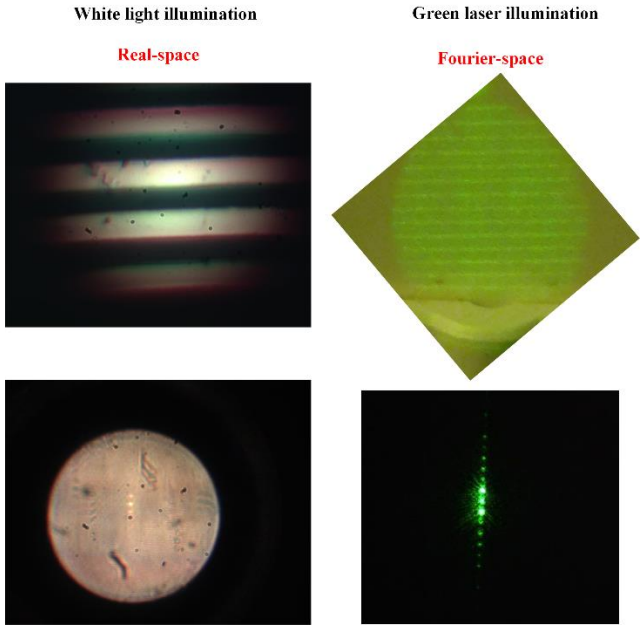


**Figure S13**. Validation of our set-up.

**References**

1. Hung, L., Lee, S. Y., McGovern, O., Rabin, O., Mayergoyz, I. (2013). Calculation and Measurement of Radiation Corrections for Plasmon Resonances in Nanoparticles. Phys. Rev. B 88, 075424.
2. Lassiter, J. B., McGuire, F., Mock, J. J., Ciracì, C., Hill, R. T., Wiley, B. J., Chilkoti, A., Smith, D. R. (2013). Plasmonic Waveguide Modes of Film-Coupled Metallic Nanocubes. Nano Lett. 13, 5866–5872.
3. Bose, S., Shendre, S., Song, Z., Sharma, V. K., Zhang, D. H., Dang, C., Fan, W., Demir, H. V. (2017). Temperature-dependent optoelectronic properties of quasi-2D colloidal cadmium selenide nanoplatelets. Nanoscale 9, 6595−6605.
4. Gao, Y.; Weidman, M. C.; Tisdale, W. (2017). A. CdSe Nanoplatelet ilms with Controlled Orientation of their Transition Dipole Moment. Nano Lett. 17, 3837−3843 (2017).
5. Scott, R., Heckmann, J., Prudnikau, A. V., Antanovich, A., Mikhailov, A., Owschimikow, N., Artemyev, M., Climente, J. I., Woggon, U., Grosse, N. B., Achtstein, A. W. (2017). Directed Emission of CdSe Nanoplatelets Originating from Strongly Anisotropic 2D Electronic Structure. Nat. Nanotechnol. 12, 1155-1160.